Possible thermochemical disequilibrium in the atmosphere of the exoplanet GJ 436b

Kevin B. Stevenson[1], Joseph Harrington[1], Sarah Nymeyer[1], Nikku Madhusudhan[2], Sara Seager[2], William C. Bowman[1], Ryan A. Hardy[1], Drake Deming[3], Emily Rauscher[4] & Nate B. Lust[1]

[1]Planetary Sciences Group, Department of Physics, University of Central Florida, Orlando, Florida 32816, USA. [2]Department of Physics and Department of Earth, Atmospheric and Planetary Sciences, Massachusetts Institute of Technology, Cambridge, Massachusetts 02159, USA. [3]Planetary Systems Laboratory, NASA Goddard Space Flight Center, Greenbelt, Maryland 20771, USA. [4]Department of Astronomy, Columbia University, New York, New York 10027, USA.

The nearby extrasolar planet GJ 436b—which has been labelled as a 'hot Neptune'—reveals itself by the dimming of light as it crosses in front of and behind its parent star as seen from Earth. Respectively known as the primary transit and secondary eclipse, the former constrains the planet's radius and mass[1,2], and the latter constrains the planet's temperature[3,4] and, with measurements at multiple wavelengths, its atmospheric composition. Previous work[5] using transmission spectroscopy failed to detect the 1.4-μm water vapour band, leaving the planet's atmospheric composition poorly constrained. Here we report the detection of planetary thermal emission from the dayside of GJ 436b at multiple infrared wavelengths during the secondary eclipse. The best-fit compositional models contain a high CO abundance and a substantial methane (CH_4) deficiency relative to thermochemical equilibrium models[6] for the predicted hydrogen-dominated atmosphere[7,8]. Moreover, we report the presence of some H_2O and traces of CO_2. Because CH_4 is expected to be the dominant carbon-bearing species, disequilibrium processes such as vertical mixing[9] and polymerization of methane[10] into substances such as ethylene may be required to explain the hot Neptune's small CH_4-to-CO ratio, which is at least 10^5 times smaller than predicted[6].

Using the Spitzer Space Telescope[11], the Spitzer Exoplanet Target of Opportunity program observed multiple secondary eclipses at wavelengths of 3.6, 4.5, 5.8, 8.0, 16 and 24 μm. Previous analyses[3,4] of our 8.0-μm secondary eclipse data confirm an eccentric orbit around GJ 436, which is a cool, M-dwarf star. Standard image calibration and photometry

produced light curves (tables of system flux versus time at each wavelength) that are available as Supplementary Information, as are details of centring and photometry. Some channels have well documented systematic effects that our Metropolis-Hastings Markov-chain Monte Carlo (MCMC) model[12] fits simultaneously with the eclipse parameters. Systematics include positional sensitivity variation[13] at 3.6, 4.5 and 5.8 µm, where the measured flux correlates with the sub-pixel location of the stellar centre, and time-varying sensitivity[14] at 4.5, 5.8, 8.0 and 16 µm. Responsivity of the 24-µm channel is relatively stable[15]. Figure 1 shows the observed secondary eclipses with best-fit models, and Table 1 presents the relevant eclipse parameters.

The phase of secondary eclipse imposes a tight constraint on the planet's eccentricity, e, and argument of periapsis, ω. Using the secondary eclipse times listed in Table 1, in addition to published transit[16] and radial-velocity data[17], a single-planet Keplerian orbit for GJ 436b has a period of 2.6438983 ± 0.0000016 days and an ephemeris time of Julian date $2,454,222.61587 \pm 0.00012$ (all errors are 1σ). These are nearly identical to the published results[16], which do not consider secondary eclipses. Using either result, the weighted average of the five measured secondary eclipse phases is 0.5868 ± 0.0003. This significant improvement from previous analyses[3,4] is due to the more precise ephemeris time and the use of multiple secondary eclipses over a long baseline. The weighted average of the minimum eccentricities, defined as $e_{min} \approx e \, \cos(\omega)$, is 0.1368 ± 0.0004. Using $\omega = 351 \pm 1.2°$ (ref. 17), we find $e = 0.1385 \pm 0.0006$. To compute all of the orbital parameters (Supplementary Information), we used the published results referenced above in addition to the eclipse times presented here. Our best-fit value for e is $0.1371^{+0.0048}_{-0.00013}$.

Our broadband observations constrain a one-dimensional atmospheric model, using a new temperature and abundance retrieval method[18]. This method searches over a wide parameter space using a functional form for the pressure–temperature profile (based on prior 'hot Jupiter' and Solar System studies), a grid of abundance combinations, and energy conservation. We calculated $\sim 10^6$ models, which considered both inversion and non-inversion temperature profiles and abundances that varied over several orders of magnitude

per constituent. Figure 2 shows two representative models (the red and blue lines) that fit the data, and Table 2 compares them to seven other objects with hydrogen-dominated atmospheres. The red model has a dayside-to-nightside energy redistribution ratio of <0.04; the blue model favours a more efficient distribution ratio of <0.31. The red model fits the data better.

Chemical equilibrium predicts H_2, H_2O, CH_4, CO and NH_3 to be the most abundant molecules in GJ 436b's atmosphere (helium must also be present but contributes minimally to the spectrum and to active chemistry). Conventional chemical composition models predict[6] the major emission contributions to come from spectroscopically active H_2O, CH_4, and, to a lesser extent, CO, and possibly CO_2. In a reduced, hydrogen-dominated atmosphere at ~700 K, CH_4 is thermochemically favoured to be the main carbon-bearing molecule. Assuming solar abundances for the elements and the pressure–temperature profile shown in Supplementary Fig. 5, chemical equilibrium predicts[6] a CH_4-to-H_2 mixing ratio of 7×10^{-4} and an H_2O mixing ratio of 2×10^{-3}. However, the strong planetary emission at 3.6 μm, combined with the non-detection at 4.5 μm, calls for a methane abundance that is depleted by a factor of ~7,000. The low H_2O abundance favoured by our red model could, in principle, result from carbon and oxygen abundances that are ~0.01 times solar values; however, the resulting CH_4 mixing ratio would still be too high, by two orders of magnitude, to explain the data.

Methane absorbs strongly in the 3.6-μm band. CO and CO_2 have absorption features at 4.5 μm, CO_2 being the stronger absorber. The high flux at 3.6 μm suggests very low absorption due to methane, while the low flux at 4.5 μm implies high absorption due to CO and/or CO_2. The degeneracy between the two molecules is solved by the low CO_2 concentration needed at 16 μm. The absence of observed flux in the 4.5-μm channel thus requires large amounts of CO, which is not expected in such a reduced atmosphere under thermochemical equilibrium, and makes a future detection at 4.5 μm important.

The flux modulation at 3.6 μm is our strongest detection, with a signal-to-noise ratio of 12.1, and has been confirmed by an independent analysis. Using 2σ error bars for this

observation and the 3σ upper limit at 4.5 µm, the low-methane requirement cannot be lifted (this result is relatively insensitive to the remaining wavelengths). An increased methane mixing ratio of 10^{-6} would result in a higher blackbody continuum, thus requiring a CO_2 mixing ratio $\geq 10^{-3}$ in order to fit the flux constraint at 4.5 µm (Figure 3). However, thermochemical equilibrium and photochemical models predict a CO_2 mixing ratio of $\sim 10^{-7}$ in hydrogen-dominated atmospheres at solar abundance ($\sim 10^{-5}$ for 30 times solar metallicities)[19,20].

We also explored other possibilities to explain the observations. A temperature inversion does not fit the data well, assuming thermochemical equilibrium, because H_2O and CH_4 would emit much more strongly than we observe in the 5.8- and 8.0-µm channels, respectively. Non-local thermodynamic equilibrium emission from the dayside of exoplanet HD 189733b is attributed[21] to CH_4 fluorescence near 3.25 µm. However, our 3.6-µm detection is too strong to be explained by fluorescence alone. Alternatively, the methane deficiency could be explained by a lack of hydrogen; however, mass and radius constraints placed by transit and radial-velocity observations call for a hydrogen-dominated atmosphere[7,8], which we explored above. Atmospheric compositions dominated by an alternative species (such as He or N_2) are difficult to invoke plausibly. Hydrogen is the most abundant species in planet-forming disks and atmospheric escape rates are small for Neptune-mass planets. Although the observations were not made simultaneously, planet variability and stellar activity are unlikely explanations for our observations. A global, planetary temperature variation of 400 K manifesting in 2.64 days (the time between the 3.6- and 4.5-µm observations) would be unprecedented in planetary science, as would a transient hot vortex[22] with one-third the planetary radius and $T \approx 2{,}200$ K that appeared during only one of our six observations. Stellar activity, which is common among M dwarfs, would need to be timed precisely with the secondary eclipse for us not to detect and mask it.

The brown dwarf GJ 570D has an effective temperature similar to that of GJ 436b (800 K), but at atmospheric levels where $T < 1{,}100$ K, CH_4 is the dominant carbon-bearing molecule, with a CH_4-to-CO ratio of $\sim 10^2$ (ref. 9). We estimate a ratio of $\leq 1 \times 10^{-3}$ for GJ

436b (Table 2); however, the exoplanet is strongly irradiated on one side, which can drive atmospheric dynamics and disequilibrium chemistry. Vertical mixing[9] can dredge CO up from deeper and hotter parts of the atmosphere, where CO is favoured, resulting in a small CH_4-to-CO ratio if the rate of dredging is faster than the rate of the reaction that converts CO to CH_4 ($CO + 3H_2 \leftrightarrow CH_4 + H_2O$). However, the observed CH_4-to-CO mixing ratio would require large amounts of vertical mixing. Alternatively, CH_4 may be depleted by polymerization into hydrocarbons such as ethylene (C_2H_4). This is a major methane reaction pathway at these temperatures[10]. These possibilities represent starting points for future theoretical work with this atmosphere.

1. Gillon, M. et al. Detection of transits of the nearby hot Neptune GJ 436 b. Astron. Astrophys. 472, L13–L16 (2007). 0705.2219.

2. Torres, G. The Transiting Exoplanet Host Star GJ 436: A Test of Stellar Evolution Models in the Lower Main Sequence, and Revised Planetary Parameters. Astrophys. J. 671, L65–L68 (2007). 0710.4883.

3. Deming, D. et al. Spitzer Transit and Secondary Eclipse Photometry of GJ 436b. Astrophys. J. 667, L199–L202 (2007). 0707.2778.

4. Demory, B.-O. et al. Characterization of the hot Neptune GJ 436 b with Spitzer and groundbased observations. Astron. Astrophys. 475, 1125–1129 (2007). 0707.3809.

5. Pont, F., Gilliland, R. L., Knutson, H., Holman, M. & Charbonneau, D. Transit infrared spectroscopy of the hot Neptune around GJ 436 with the Hubble Space Telescope. Mon. Not. R. Astron. Soc. 393, L6–L10 (2009). 0810.5731.

6. Burrows, A. & Sharp, C. M. Chemical Equilibrium Abundances in Brown Dwarf and Extrasolar Giant Planet Atmospheres. Astrophy. J. 512, 843–863 (1999). arXiv:astro-ph/9807055.

7. Figueira, P. et al. Bulk composition of the transiting hot Neptune around GJ 436. Astron. Astrophys. 493, 671–676 (2009). 0904.2979.

8. Rogers, L. A. & Seager, S. A Framework for Quantifying the Degeneracies of Exoplanet Interior Compositions. ArXiv e-prints (2009). 0912.3288.

9. Saumon, D. et al. Ammonia as a Tracer of Chemical Equilibrium in the T7.5 Dwarf Gliese 570D. Astrophy. J. 647, 552–557 (2006). arXiv:astro-ph/0605563.

10. Zahnle, K., Marley, M. S. & Fortney, J. J. Thermometric Soots on Hot Jupiters? ArXiv e-prints (2009). 0911.0728.

11. Werner, M. W. et al. The Spitzer Space Telescope Mission. Astrophy. J. Suppl. Ser. 154, 1–9 (2004). arXiv:astro-ph/0406223.

12. Ford, E. B. Quantifying the Uncertainty in the Orbits of Extrasolar Planets. Astrophys. J. 129, 1706–1717 (2005). arXiv:astro-ph/0305441.

13. Knutson, H. A., Charbonneau, D., Allen, L. E., Burrows, A. & Megeath, S. T. The 3.6-8.0 μm Broadband Emission Spectrum of HD 209458b: Evidence for an Atmospheric Temperature Inversion. Astrophys. J. 673, 526–531 (2008). 0709.3984.

14. Harrington, J., Luszcz, S., Seager, S., Deming, D. & Richardson, L. J. The hottest planet. Nature 447, 691–693 (2007).

15. Deming, D., Seager, S., Richardson, L. J. & Harrington, J. Infrared radiation from an Extrasolar planet. Nature 434, 740–743 (2005). arXiv:astro-ph/0503554.

16. Caceres, C. et al. High Cadence Near Infrared Timing Observations of Extrasolar Planets: I. GJ 436b and XO-1b. ArXiv e-prints (2009). 0905.1728.

17. Maness, H. L. et al. The M Dwarf GJ 436 and its Neptune-Mass Planet. Publ. Astron. Soc. Pac. 119, 90–101 (2007). arXiv:astro-ph/0608260.

18. Madhusudhan, N. & Seager, S. A Temperature and Abundance Retrieval Method for Exoplanet Atmospheres. Astrophys. J. 707, 24–39 (2009). 0910.1347.

19. Lodders, K. & Fegley, B. Atmospheric Chemistry in Giant Planets, Brown Dwarfs, and Low-Mass Dwarf Stars. I. Carbon, Nitrogen, and Oxygen. Icarus 155, 393-424 (2002)

20. Zahnle, K., Marley, M. S., Freedman, R. S., Lodders, K. & Fortney, J. J. Atmospheric Sulfur Photochemistry on Hot Jupiters. Astrophy. J. Lett. 701, L20–L24 (2009). 0903.1663.

21. Swain, M. R. et al. A ground-based near-infrared emission spectrum of the exoplanet HD189733b. Nature 463, 637-639 (2010).

22. Cho, J., Menou, K., Hansen, B. M. S. & Seager, S. Atmospheric Circulation of Close-in Extrasolar Giant Planets. I. Global, Barotropic, Adiabatic Simulations. Astrophys. J. 675, 817–845 (2008).

23. Alonso, R. et al. Limits to the planet candidate GJ 436c. Astron. Astrophys. 487, L5–L8 (2008). 0804.3030.

24. Castelli, F. & Kurucz, R. L. New Grids of ATLAS9 Model Atmospheres. ArXiv Astrophysics e-prints (2004). arXiv:astro-ph/0405087.

25. Bean, J. L., Benedict, G. F. & Endl, M. Metallicities of M Dwarf Planet Hosts from Spectral Synthesis. Astrophys. J. 653, L65–L68 (2006). arXiv:astro-ph/0611060.

26. Swain, M. R. et al. Molecular Signatures in the Near-Infrared Dayside Spectrum of HD 189733b. Astrophy. J. Lett. 690, L114–L117 (2009).

27. Atreya, S. K., Mahaffy, P. R., Niemann, H. B., Wong, M. H. & Owen, T. C. Composition and origin of the atmosphere of Jupiter-an update, and implications for the extrasolar giant planets. Planet. Space Sci. 51, 105–112 (2003).

28. Lodders, K. & Fegley, B., Jr. The origin of carbon monoxide in Neptunes's atmosphere. Icarus 112, 368–375 (1994).

29. Mandel, K. & Agol, E. Analytic Light Curves for Planetary Transit Searches. Astrophys. J. 580, L171–L175 (2002). arXiv:astro-ph/0210099.

30. Reiners, A. Activity-induced radial velocity jitter in a flaring M dwarf. Astron. Astrophys. 498, 853–861 (2009). 0903.2661.

Supplementary Information is linked to the online version of the paper at www.nature.com/nature.

Author Contributions K.B.S. wrote the paper and Supplementary Information with contributions from J.H., N.M. and R.A.H.; N.M. and S.S. produced the atmospheric models; S.N., K.B.S. and W.C.B. reduced the data; K.B.S., J.H. and D.D. analysed the results; D.D. ran an independent analysis; R.A.H. produced the orbital parameter results; and J.H., K.B.S., S.N., R.A.H., E.R. and N.B.L. wrote the analysis pipeline.

Author Information The original data are available from the Spitzer Space Telescope archive, programs 30129 and 40685. Reprints and permissions information is available at www.nature.com/reprints. The authors declare no competing financial interests. Correspondence and requests for materials should be addressed to K.B.S. (kevin218@knights.ucf.edu).
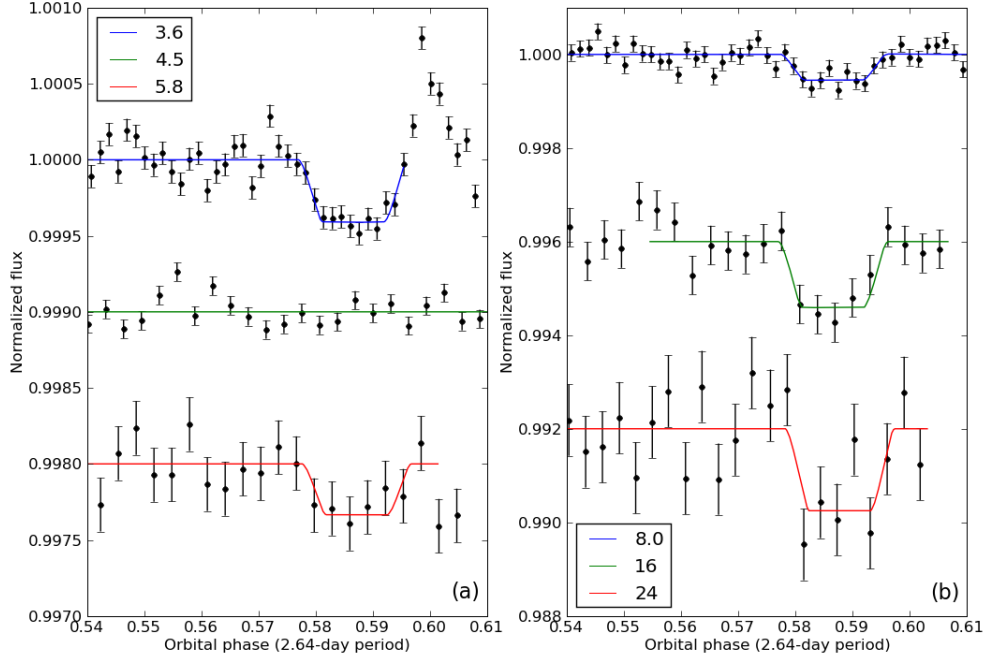
Figure 1. Secondary eclipses of GJ 436b at six Spitzer wavelengths. The flux values are corrected for sensitivity effects, normalized to the system brightness, and vertically separated for ease of comparison. **a**, Binned 3.6-, 4.5- and 5.8-µm data (with 1σ error bars), **b**, binned 8.0-, 16- and 24-µm data (with 1σ error bars), both with best-fit models and for orbital phases greater than 0.54. Note the different vertical scales used in each panel. The phase calculation uses an ephemeris time of Julian date 2,454,222.61588 and a period of 2.6438986 days (ref. 16). Because the planet passes behind the star, we ignore stellar limb darkening and use the uniform-source equations[29] for the eclipse shape. The position sensitivity model used either a quadratic[13] or a cubic function in the two spatial variables, including the cross terms to account for any correlation. An asymptotically constant exponential function[14] models the time-varying sensitivity. The 3.6- and 4.5-µm channels exhibit strong position sensitivity while the 5.8-µm channel reveals a weak correlation with pixel position. The unmodelled region at 3.6 µm may be the result of stellar activity[30]; a similar region at 5.8 µm is unmodelled for reasons presented in Supplementary

Information. We detect no eclipse at 4.5 μm, but constrain the flux modulation at its 3σ upper bound by fixing the secondary eclipse phase to the mean weighted value of the other channels. We use asymptotically constant exponential and linear functions to model the time-varying sensitivities at 8.0 and 16 μm, respectively. Our 8.0-μm analysis agrees with prior analyses[3,4] but we obtain a slightly higher brightness temperature (Table 1) due, in part, to a more recent Kurucz model[24]. No correction is necessary at 24 μm.
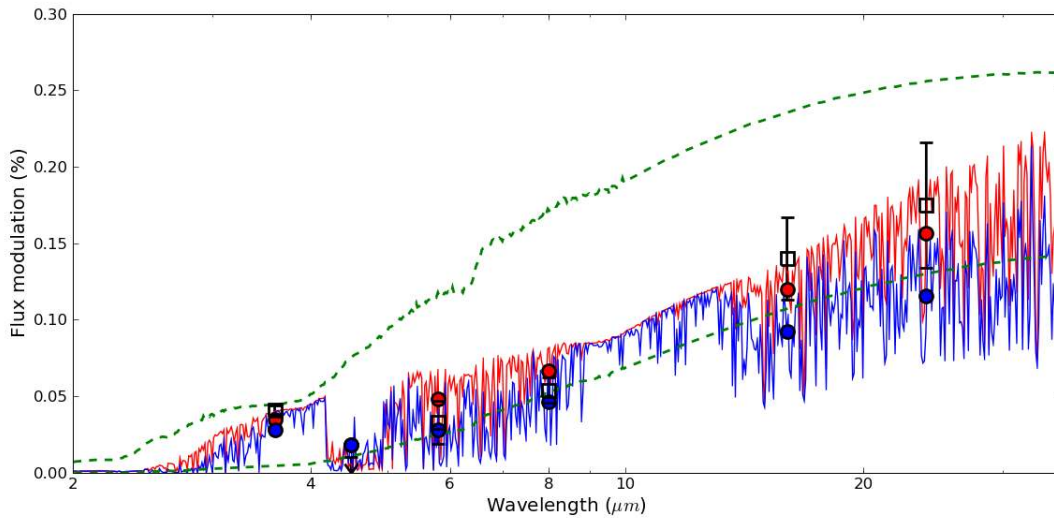
Figure 2. Broadband spectrum constraints for GJ 436b. The two atmospheric models (red and blue lines) have the same temperature structure and no thermal inversion. The red model has uniform mixing ratios for H_2O, CH_4, CO and CO_2 of 3×10^{-6}, 1×10^{-7}, 7×10^{-4} and 1×10^{-7}, respectively. For the blue model, these are 1×10^{-4}, 1×10^{-7}, 1×10^{-4} and 1×10^{-6}. The 3.6-μm channel is the key measurement in terms of constraining the methane abundance. It also limits the amount of H_2O to less than that of CO, with little to no energy redistribution. Chemical equilibrium also requires some NH_3. The coloured circles are the bandpass-integrated models, the black squares are our data (with 1σ error bars), and the black arrow depicts the 3σ upper limit at 4.5 μm. The dashed green curves show blackbody spectra at 650 K (bottom) and 1,050 K (top) divided by the Kurucz stellar spectrum model[24]. The red and blue models have effective (equivalent blackbody) temperatures of

860 K and 790 K, respectively. We need not invoke an internal heat source[3]. Assuming zero albedo and planet-wide redistribution of heat, GJ 436b has an equilibrium temperature (T_{eq}, where emitted and absorbed radiation balance for an equivalent blackbody) of 770 K at periapse. For instantaneous reradiation of absorbed energy at secondary eclipse, the hemispheric effective temperature is 800 K and the peak temperature is 1,030 K.
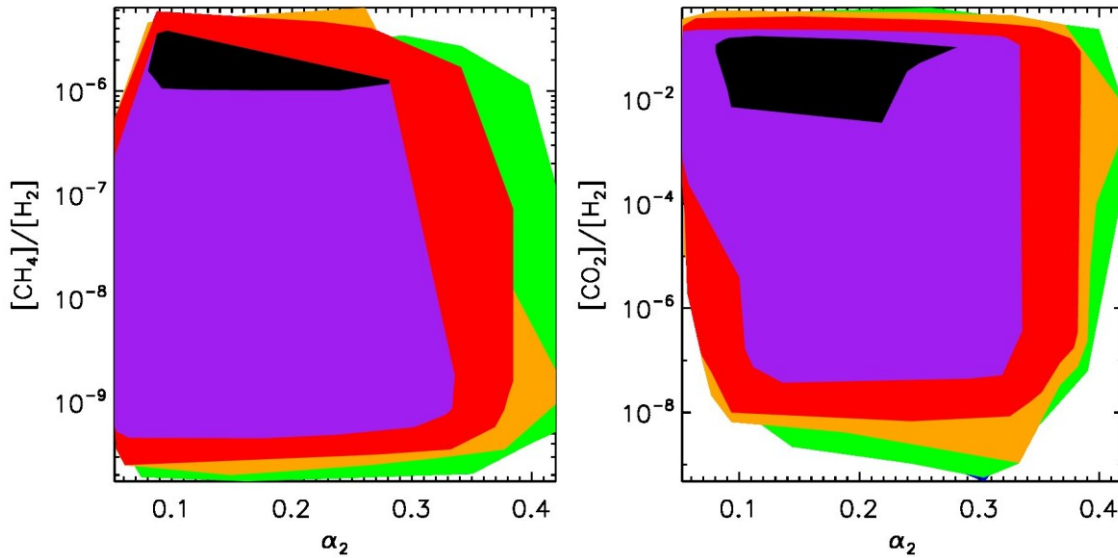
Figure 3. Contours showing the explored mixing ratios of methane. The purple, red, orange and green contours show error surfaces within ξ^2 of 1, 2, 3 and 4, where ξ^2 is χ^2 divided by the number of channels. We use the 3σ upper limit for the 4.5-μm observation. The black surfaces show models with $\xi^2 < 1$ and $CH_4/H_2 > 10^{-6}$. The figure demonstrates that models with CH_4 mixing ratios close to 10^{-6} or above (panel **a**) require extremely large ($>10^{-3}$) CO_2 mixing ratios (panel **b**), which are unphysical based on current understanding of CO_2 photochemistry. The parameter space was explored with $\sim 10^6$ models. The α_2 parameter, which is related to the temperature gradient in the lower atmosphere[18], was chosen arbitrarily for the abscissa.

Table 1. Eclipse parameters and brightness temperatures

Channel (μm)	Eclipse midpoint (BJD − 2454000)	Eclipse duration (orbits)	Flux modulation (%)	Brightness temperature (K)
3.6	496.4888 ± 0.0010	0.0192 ± 0.0008	0.041 ± 0.003	1,120 ± 20
4.5	499.1330	0.0191	<0.010*	<700
5.8	501.778 ± 0.005	0.0191	0.033 ± 0.014	720 ± 110
8.0	282.3331 ± 0.0016	0.0186 ± 0.0014	0.054 ± 0.008	740 ± 40
16	477.981 ± 0.003	0.0191 ± 0.0023	0.140 ± 0.027	980 ± 130
24	470.053 ± 0.002	0.0191	0.175 ± 0.041	960 ± 170

BJD, barycentric Julian date; 1 orbit = 2.6438986 days. Eclipse duration is measured from start of ingress (t_1) to end of egress (t_4). Flux modulation is one minus in-eclipse flux divided by out-of-eclipse flux. Brightness temperature is the temperature of a similar blackbody that produces the same flux as the source in a given wavelength bandpass. The eclipses at 3.6, 8.0 and 16 μm are clear enough to fit durations; their weighted mean (72.6 ± 2.6 min) fixes the durations for the other wavelengths. We fix the ingress/egress times to 16 min (ref. 23) for all channels. Varying them produces equivalent times within the errors but degrades the overall fit quality. The Supplementary Tables and Supplementary Figures contain complete parameter results. The brightness temperature calculation[14] refers the flux modulation to a stellar spectrum model, which is interpolated from a grid of Kurucz models[24] using GJ 436's temperature (3,684 ± 71 K), log surface gravity (4.80 ± 0.10), and metallicity (−0.32 ± 0.12 dex)[2,25]. A Monte Carlo method computes the uncertainty in brightness temperature by varying the flux modulation and stellar parameters. The differing brightness temperatures at 3.6 and 4.5 μm suggest that these two wavelengths measure two different pressure levels; indeed Supplementary Fig. 5 shows that the 4.5-μm channel has an additional contribution from higher up in the atmosphere. To explain the 400 K difference in brightness temperatures, the model requires a very low concentration of methane.

*3σ upper limit.

Table 2. Atmospheric data for various planets

Planet	H_2O	CH_4	CO	CO_2	T_{eff} (K)	CH_4/CO
HD 209458b[18] (Spitzer broadband)	$\geq 10^{-8}$ $\leq 10^{-5}$	$\geq 4 \times 10^{-8}$ $\leq 3 \times 10^{-2}$	$\geq 4 \times 10^{-4}$	$\geq 4 \times 10^{-9}$ $\leq 7 \times 10^{-8}$	$\geq 1{,}310$ $\leq 1{,}690$	$\gtrsim 10^{-7}$ $\lesssim 10^{2}$
HD 189733b[18] (Spitzer broadband)	$\geq 10^{-5}$ $\leq 10^{-3}$	$\leq 2 \times 10^{-6}$	$\geq 7 \times 10^{-8}$ $\leq 2 \times 10^{-2}$	$\geq 7 \times 10^{-7}$ $\leq 7 \times 10^{-5}$	$\geq 1{,}480$ $\leq 1{,}560$	$\gtrsim 10^{-10}$ $\lesssim 10$
HD 189733b[26] (HST/NICMOS)	$\geq 1 \times 10^{-4}$ $\leq 1 \times 10^{-3}$	$\leq 1 \times 10^{-7}$	$\geq 1 \times 10^{-4}$ $\leq 3 \times 10^{-4}$	$\geq 1 \times 10^{-6}$ $\leq 1 \times 10^{-5}$	NA	$\lesssim 10^{-3}$
GJ 436b (red)	3×10^{-6}	1×10^{-7}	7×10^{-4}	1×10^{-7}	860	$\sim 10^{-4}$
GJ 570D[2]	7×10^{-4}	5×10^{-4}	2×10^{-6}	NA	800	$\sim 10^{2}$
GJ 436b (blue)	1×10^{-4}	1×10^{-7}	1×10^{-4}	1×10^{-6}	790	$\sim 10^{-3}$
Jupiter[27]	$\geq 2 \times 10^{-9}$ $\leq 2 \times 10^{-8*}$	2.1×10^{-3}	1.6×10^{-9}	$\leq 3 \times 10^{-9}$	110	$\sim 10^{6}$
Saturn[27]	$\geq 2 \times 10^{-9}$ $\leq 2 \times 10^{-8*}$	4.5×10^{-3}	1×10^{-9}	3×10^{-10}	100	$\sim 10^{6}$
Uranus[28]	Ice	2.3×10^{-2}	$\leq 1.2 \times 10^{-8}$	NA	60	$\sim 10^{6}$
Neptune[28]	Ice	2.9×10^{-2}	$\sim 1 \times 10^{-6}$	NA	60	$\sim 10^{4}$

Values given under headings H_2O, CH_4, CO and CO_2 are mixing ratios relative to hydrogen. T_{eff}, effective temperature; HST/NICMOS, Hubble Space Telescope Near Infrared Camera and Multi-Object Spectrometer. The planets are ordered in descending effective temperature. Chemical equilibrium predicts a roughly increasing CH_4-to-CO ratio. GJ 436b does not follow this general trend, as seen in the rightmost column. Its CH_4-to-H_2 mixing ratio is $>10^3$ times less than that of a brown dwarf of similar temperature and its CH_4-to-CO ratio is $>10^5$ times less. Excess CO may be the result of relatively strong vertical mixing[9]. A significant fraction of the methane may have polymerized into hydrocarbons[10], resulting in a shortage in observed CH_4. For comparison, GJ 436b's required methane mixing ratio of 10^{-7} is about 10^5 times less than that on Uranus and Neptune, 10^4 times less than that on Jupiter and Saturn, and ~20 times less than that on Earth, where methane is oxidized, not polymerized. NA, not available.
*Above cloud.

Supplementary Information

At a relative flux level of just ~0.1% compared to the host star, exoplanet secondary eclipses are well below Spitzer's 2% relative photometric accuracy requirement[31]. This and their low intrinsic signal-to-noise ratios (SNR, often below 10) require that we attend closely to analysis details. Because different analysis approaches may obtain significantly different results, we also present more than the usual level of detail about our fits, so that future investigators who choose to analyze these data can compare their work to ours. This Supplementary Information (SI) presents how we determined the centres of the photometric apertures, adjusted for varying array sensitivity with respect to aperture centre location ("position sensitivity") and time ("ramp"), and fit models to the data. The final section presents the results of our fits in sufficient detail for evaluation of alternative analyses. Many other methods appear in the SI to Ref. 14.

Centring and Photometry

Spitzer's instrumental point-spread functions (PSFs) are stable in time and vary little with the normal pointing wander (<1") over a few-hour staring observation. Since zodiacal light and instrumental effects contribute significant noise, we use a small aperture plus an aperture correction at short wavelengths and optimal photometry[15,32] at longer wavelengths. In either case, mismatching the aperture or PSF model to the data produces additional error, so one must determine PSF centres accurately. Here we compare three methods. The first[33] computes the centre of light of pixels within a circular aperture and above the frame's median value by at least 0.1% of the median-subtracted peak value. The second fits a two-dimensional (2D) Gaussian with free position parameters. The third, called least asymmetry, optimizes the stellar radial profile by calculating:

$$\text{Asym } (x,\ y) = \sum_{i=1}^{i_{max}} n_{r_i} \sigma_{r_i}^{4} \ , \tag{1}$$

where (x, y) is the current pixel location and σ_r is the standard deviation of the n_r pixels at the radial distance r_i in pixels from the current central pixel. The first few discrete values for r_i are 1, $\sqrt{2}$, 2, $\sqrt{5}$, $2\sqrt{2}$, 3, etc. We find using $i_{max} = 5$ provides comparable precision and computes faster than larger values. An inverted 2D Gaussian with free position parameters finds the minimum in asymmetry space, which defines the centre of the object.

Tests using real datasets show that the 2D Gaussian and least-asymmetry methods are more precise than the centre-of-light method (see Supplementary Figure 1). For the example data, the Gaussian method is the most precise, but this is not always true. We tested the accuracy with a fake dataset made from a 100× oversampled Spitzer Point Response Function[34] (PRF) centred at 50 locations along a pixel diagonal. We rebinned each image to the nominal resolution, copied it 100 times, and added Gaussian noise. Supplementary Figure 2 plots the median residuals between the known and computed centres for the Gaussian and least-asymmetry methods. Both methods are comparable near the corners, but the least-asymmetry method is more accurate near a pixel centre. The Gaussian method is more consistent over the entire pixel range. For the observations of GJ 436b at 5.8 and 8.0 μm, the mean radial distances from their respective pixel centres are ~0.2 pixels, so, as indicated in Supplementary Table 1, the best centring method is least asymmetry. The evaluation metric is the standard deviation of the normalized (with respect to the stellar flux) residuals between the measured and model flux values.

The IRS and MIPS channels typically achieve their best results using optimal photometry, but 5×-interpolated aperture photometry[14] is best for the IRAC channels. Supplementary Table 1 gives the best aperture sizes, found by varying the size and minimizing the standard deviation of the normalized residuals. Changing the aperture size by 0.25 pixels from the best value increases this standard deviation by <0.4% and typically by much less, so smaller pixel increments are unnecessary.
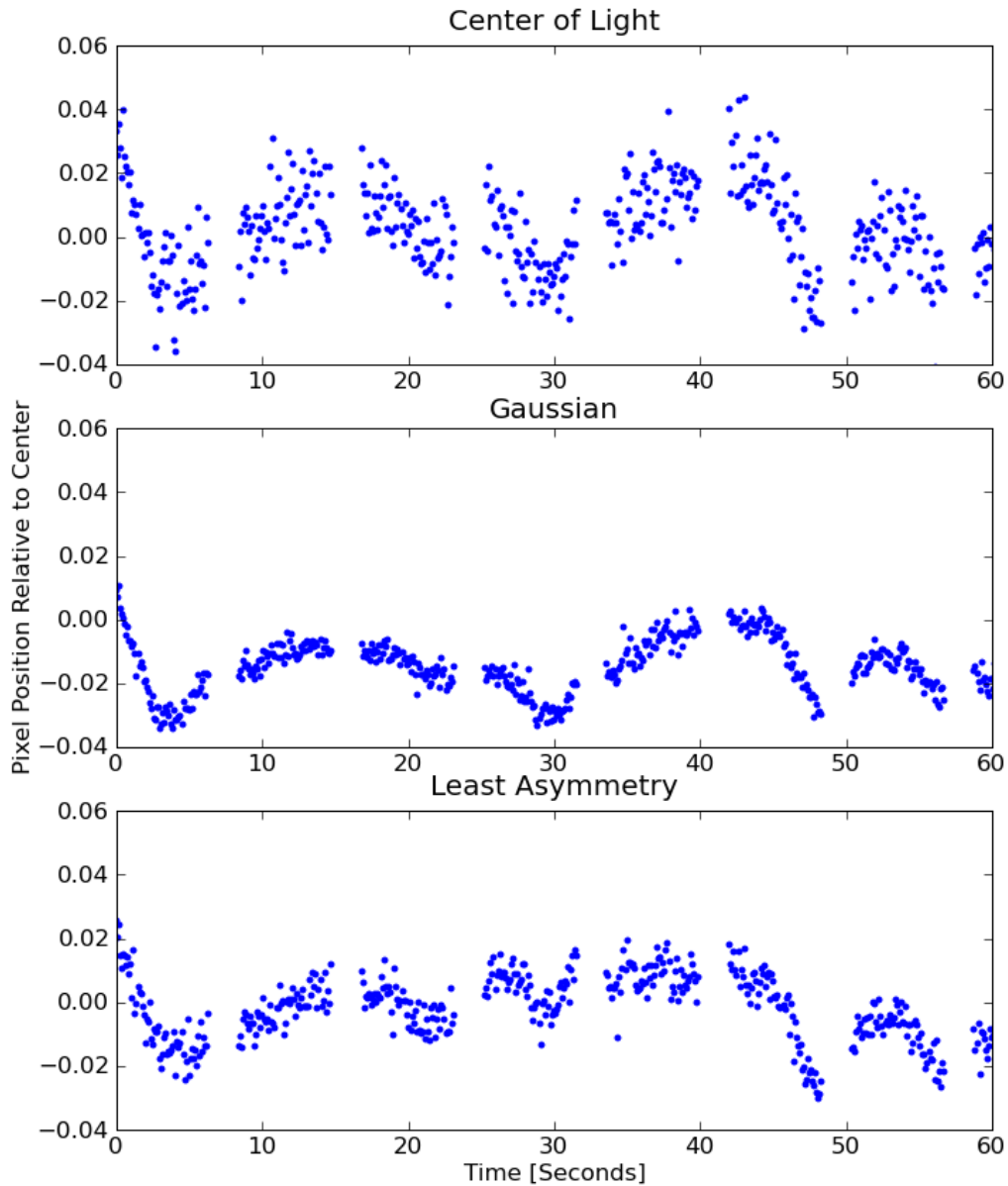
Supplementary Figure 1. Three centring methods track the vertical position of GJ 436b for a small portion of the 3.6 μm data. For this dataset, the Gaussian centring method most precisely tracks the spacecraft pointing. Small pointing oscillations occur on a ~5-second timescale. Gaps occur every 64 frames as the camera transfers data to the spacecraft's data system.
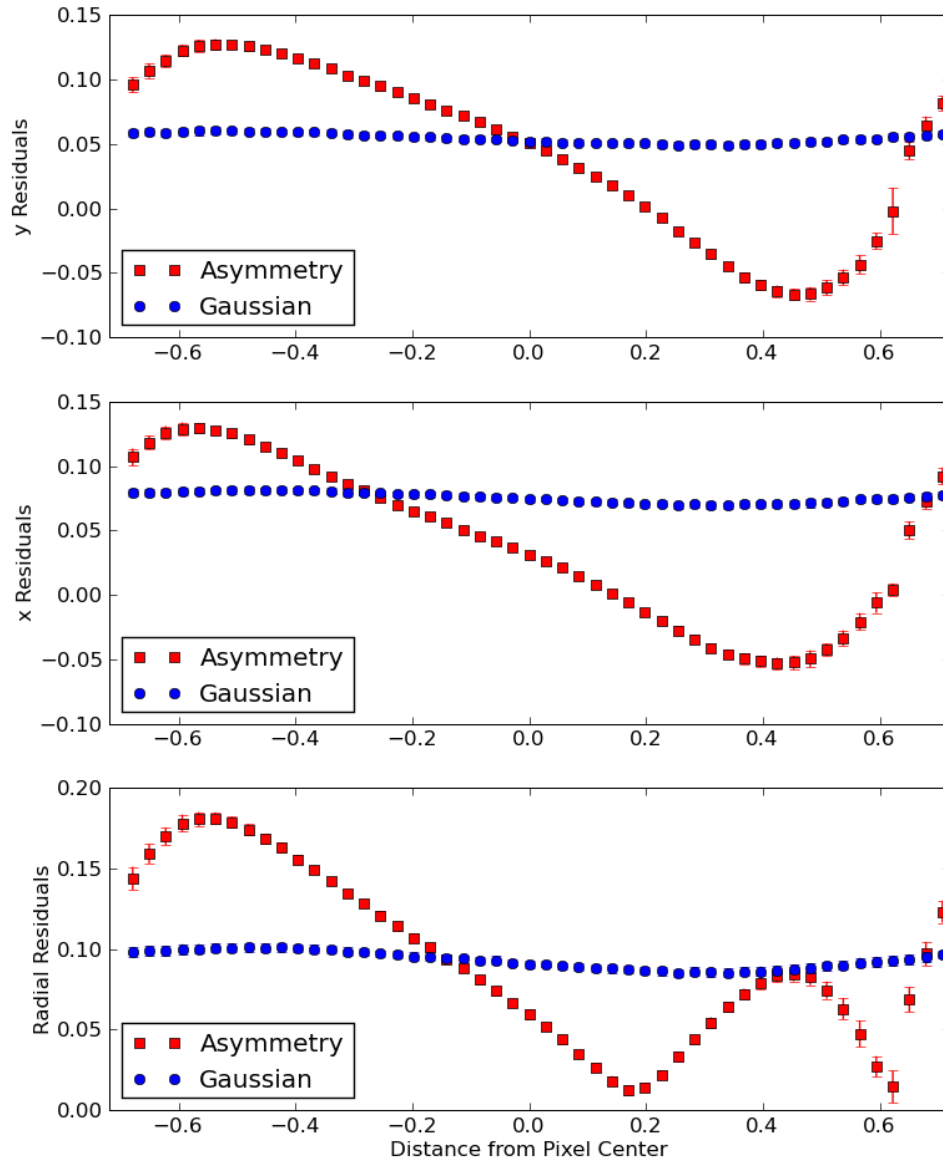
Supplementary Figure 2. Comparison between Gaussian and least-asymmetry centring methods. Each point (1σ error bars) represents the median and standard deviation of the y (top), x (middle), and radial (bottom) residuals between the known and measured centroids using 100 synthetic PRF images, each with Gaussian noise, having true centres at the diagonal distances given along the abscissa. The least asymmetry method consistently outperforms the Gaussian method when the true centroid is close to the centre of the pixel. The Spitzer PRFs are not perfectly symmetric, resulting in the asymmetric form of the plots across the pixel centre.

Supplementary Table 1. Centring method and photometry apertures.

Channel [μm]	Camera	Centring Method	Aperture Size [Pixels]
3.6	IRAC	Gaussian	2.75
4.5	IRAC	Gaussian	4.75
5.8	IRAC	Least Asymmetry	3.25
8.0	IRAC	Least Asymmetry	3.75
16	IRS	Gaussian	N/A
24	MIPS	Gaussian	N/A

IRAC = Infrared Array Camera[31].

IRS = Infrared Spectrograph (blue peak-up array)[35].

MIPS = Multiband Imaging Photometer for Spitzer[36].

Position Sensitivity

In the 3.6- and 4.5-μm Spitzer channels, sensitivity varies up to 3.5% with centroid position. We detect for the first time much smaller variations at 5.8 μm, which may be due to intra-pixel sensitivity variations or residual flat-field errors. Polynomial models in the two position variables fit the position sensitivity:

$$\varphi' = \varphi\left[ay^2 + bx^2 + cyx + dy + ex + 1\right] \tag{2}$$

$$\varphi' = \varphi\left[ay^3 + bx^3 + cy^2x + dyx^2 + ey^2 + fx^2 + gyx + hy + ix + 1\right] \tag{3}$$

where ϕ' and ϕ are the measured and corrected fluxes, respectively, x and y denote the PSF centre relative to the pixel centre, and $a - i$ are (potential) free parameters. In general (but not for these particular datasets), if many of the PSF centres fall on two or more pixels, the sensitivity difference between pixels (uncorrected flat field) becomes important. In this case, each of the visited pixels has its own correction.

Time-Varying Sensitivity

Two functions model the time-varying sensitivity: an asymptotically constant exponential[14] and a combination of logarithmic plus linear functions (similar to Ref. 3):

$$\varphi' = \varphi \cdot \left[1 \pm \exp \left\{ - a \cdot (t - t_0) \right\} \right] \qquad\qquad (4)$$

$$\varphi' = \varphi \cdot \left[a \cdot \ln (t - t_0) + b \cdot (t - t_0) + 1 \right], \qquad\qquad (5)$$

where, in Eqn. 4, the positive and negative signs are used for exponentially decreasing and increasing variability, t is the observation time, and the free parameters are a, b, and t_0. If both intra-pixel and time-varying sensitivities apply, their multiplied corrections use only one ϕ. Although ϕ' in Eqn. 5 tends toward infinity at large t, this physical impossibility is not a problem for observations of a few hours. Eqn. 4 curves more, so it generally produces slightly deeper eclipses than Eqn. 5. Without any physical reason to prefer either function, we test both and report the one with the lowest Bayesian Information Criterion value (described below).

Determining the Best Model

The Metropolis-Hastings algorithm, a specific Markov-Chain Monte Carlo (MCMC) method[12], explores the model phase space to estimate the values and uncertainties of the free parameters. The position sensitivity, time-varying sensitivity, and eclipse model elements evaluate simultaneously. The eclipse element has parameters for the phase of secondary eclipse (the fraction of one orbital period from mid-transit to mid-eclipse), the duration between the first and fourth contact points, the eclipse flux ratio (or modulation, one minus the in- versus out-of-eclipse flux values), the ingress and egress durations, and ϕ in the absence of any sensitivity model elements. These parameters define the shape of the eclipse following Ref. 29 for a uniform source. Spitzer Basic Calibrated Data (BCD) come with calculated flux uncertainties per pixel, which are typically too large[14]. After a "burn-

in" of at least 10^5 iterations to forget the starting conditions, we rescale the uncertainties to give a reduced χ^2 of ~ 1. After 10^6 or more iterations, the best-fit parameters are those with the least χ^2 value. We calculate the 34th percentile in both directions from the median value to obtain uncertainties (averaged if close, quoted separately otherwise).

The Bayesian Information Criterion (BIC)[37,38] compares models with differing numbers of free parameters, heavily penalizing those with more, relative to the least χ^2 method. The preferred model has the lowest BIC value:

$$\text{BIC} = \frac{1}{\sigma^2} \sum_{i=1}^{n} \varepsilon_i^2 + k \cdot \ln\{n\}, \qquad (6)$$

where ε_i and is the residual of the ith data point, σ^2 is the error variance, n is the number of data points, and k is the number of free parameters. Supplementary Table 2 lists the combinations of model elements used in each channel, the resulting standard deviation of the normalized residuals, and the BIC values. Position sensitivity terms that contribute negligibly to the fit are removed from the model. The type of position sensitivity model element used does not significantly affect the eclipse parameters but can reduce their uncertainties.

Supplementary Discussion

The short-lived spike that occurred after the eclipse at 3.6 μm may be the result of stellar activity[30,39]. If this sharp increase in observed flux had affected the eclipse, the flux ratio would have been larger and the duration longer, thus requiring even lower levels of methane in the models and an inexplicably long duration. We contend that this is not the case and do not fit the affected points. The high interest in M-dwarf planets calls for observational study of M-dwarf activity, notably flares, across the spectrum.

Supplementary Table 2. Eclipse free parameters and best models

Channel [μm]	Eclipse Free Parameters	Time-Varying Sensitivity	Position Sensitivity	Std. Dev. Of Norm. Residuals	BIC
3.6	Depth, Duration, Phase	-	Quadratic	0.003839	100548
			Cubic	0.003830	100136
4.5	Depth	Falling Exponential	Quadratic	0.002449	37738
			x^2, x & y terms only	0.002450	37718
5.8	Depth, Phase	Falling Exponential	-	0.007208	35423
			Quadratic	0.007194	35335
			y^2 term only	0.007194	35293
8.0	Depth, Duration, Phase	Rising Exponential	-	0.004985	37802
		Log + Linear	-	0.004984	37809
16	Depth, Duration, Phase	Linear	-	0.002939	875
		Quadratic	-	0.002923	1022
24	Depth, Phase	-	-	0.006344	1179

The residuals are normalized to the stellar flux.

The last ~2500 photometry points (~5%) at 5.8 μm drop unexpectedly and are difficult to model. Including these values in the fit causes the best-fit flux ratio to decrease from 0.033% to 0.020% using the quadratic position sensitivity model. In addition, the eclipse phase changes drastically with the additional points, resulting in relatively large errors. The weaker flux ratio is comparable in magnitude to the remaining deviations from the model, attracting the Metropolis-Hastings algorithm to nearby local minima that mimic eclipses. Without the position sensitivity model, the best fit has a physically impossible negative flux ratio. By fixing the eclipse phase, as we did for the 4.5-μm photometry, the flux ratio histogram of the MCMC trials are Gaussian distributed (see below); however, the ramp curvature and phase offset parameters possess distinct bimodal distributions with

standard deviations ~5 times larger than leaving the eclipse phase as a free parameter. We exclude these points from the final model.

The 5.8 and 8.0 μm channels use Si:As detectors and are not expected to have intra-pixel sensitivity variations like the In:Sb detectors for the 3.6- and 4.5-μm channels[13]. Nonetheless, the weak position sensitivity effect at 5.8 μm clearly improves the fit, as indicated by the lower BIC value in Supplementary Table 2 and as shown in Supplementary Figure 3. The oscillatory motion of the flux (top panel) is in phase with that of the position on the detector (bottom panel) and the best-fit curve mimics the flux motion with high precision. This may be due to intra-pixel sensitivity or uncorrected flat field errors. A possible micrometeoroid impact caused a sudden shift in position at phase = 0.58 (BJD = 2454501.7555). This did not affect the measured flux values, so we did not remove any frames from this event that were not already flagged as bad. There are small oscillations in the flux at 8.0 μm, but we find no correlation between flux and position.

The relative dependences of position sensitivity on the measured flux are apparent at the three lowest wavelengths in Supplementary Figure 4. The time-varying sensitivities[14] at 5.8, 8.0, and 16 μm are also evident. Previous analyses[3,4] at 8.0 μm used log plus linear and asymptotic exponential functions, respectively, to model the time-varying sensitivity. We use the latter, which typically results in slightly larger flux ratios compared to the log-plus-linear expression. The pixel sensitivity at 16 μm increases by ~1.5% until the phase reaches 0.54. It then stabilizes before decreasing in sensitivity. We only model the decreasing section, using a linear function. Other models produced larger BIC values. The mean images in the MIPS dataset, with bad pixels removed, revealed a clear, roughly quadratic rise in the background level along the y axis. This effect varied with position but was consistent at each scan mirror tilt angle. We thus subtracted the median value along the x-axis from each row of each image. However, the photometric results from the background-subtracted images did not show improvement, so we used the uncorrected data.
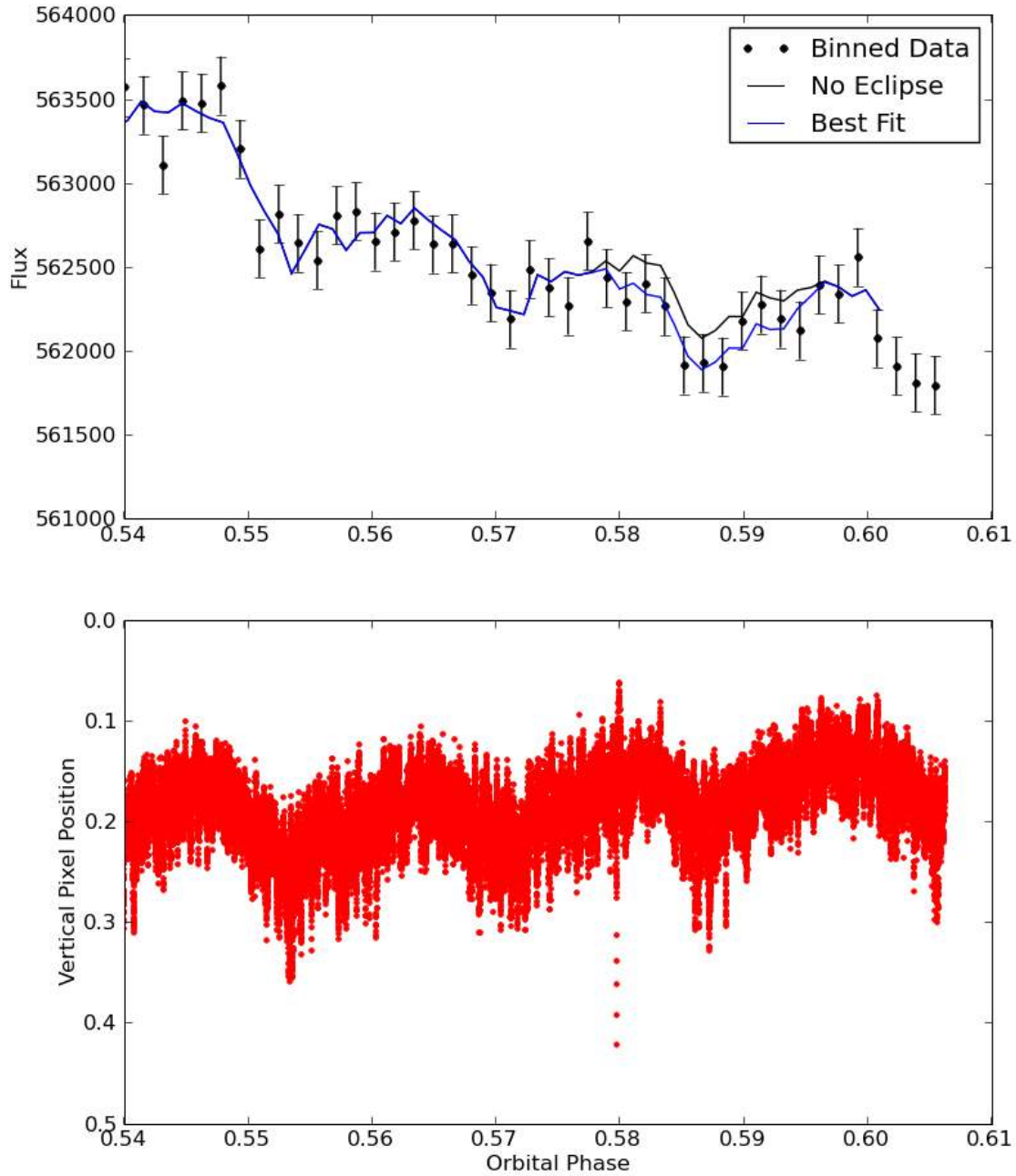
Supplementary Figure 3. **Position sensitivity at 5.8 μm.** The top panel plots the binned fluxes and best-fit model *vs.* phase. The bottom panel shows the unbinned vertical pixel positions (least asymmetry method, Gaussian is similar), which correlate with the measured flux values. Note the position excursion – possibly a micrometeoroid hit – at phase ~0.58.
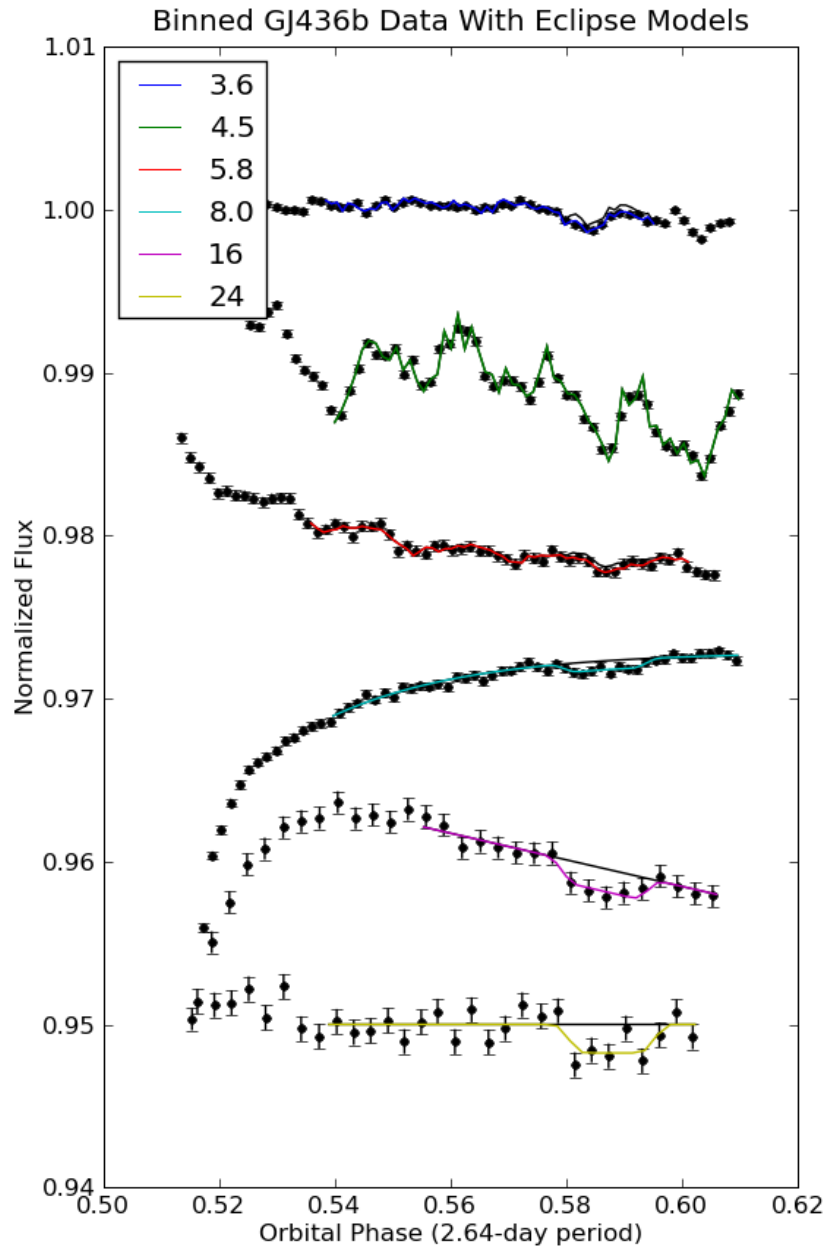
**Supplementary Figure 4. Binned, normalized, raw photometry of the GJ 436 system
in all six channels with eclipse and systematic models.** The channels are vertically offset
for clarity. The black curves do not include the eclipse model elements. At 4.5 μm, the
eclipse depth is too small to distinguish.

Supplementary Tables

Supplementary Table 3. Best-fit orbital parameters with corresponding errors.

Parameter	Best Fit	Error
Period (Days)	2.6438983	± 0.0000016
Ephemeris Time (JD)	2454222.61587	± 0.00012
Argument of Periapsis (°)	357	± 10.
Eccentricity	0.1371	+ 0.0048 - 0.00013
Semi-Amplitude (m/s)	18.2	± 0.4
Linear Slope (m/s/yr)	1.27	± 0.20
Linear Offset (m/s)	4.1	± 0.7

We used published transit[16] and RV[17] data but removed two points due to the Rossiter-McLaughlin effect[40]. Our MCMC orbit routine fit the period, ephemeris time, argument of periapsis (ω), eccentricity (e), semi-amplitude (K), a linear correction slope (dv/dt), and an offset (γ) term.

Supplementary Table 4. Best-fit free parameters at 3.6 μm.

Parameter	Best Fit	Low Error	High Error	SNR
Eclipse Phase [orbits]	0.5867	-0.0004	0.0004	1,600
Eclipse Duration [orbits]	0.0192	-0.0008	0.0008	23.0
Flux Ratio [%]	0.041	-0.003	0.003	12.1
Star Flux [μJy]	1,287,800	-500	600	2,350
Intra-pixel, Cubic Term in y	0.11	-0.02	0.02	5.3
Intra-pixel, Cubic Term in x	-0.057	-0.004	0.004	12.8
Intra-pixel, y^2x Cross Term	0.12	-0.02	0.04	3.9
Intra-pixel, yx^2 Cross Term	0.185	-0.035	0.014	7.5
Intra-pixel, Quadratic Term in y	-0.710	-0.04	0.05	15.1
Intra-pixel, Quadratic Term in x	-0.0200	-0.0020	0.0017	10.9
Intra-pixel, yx Cross Term	-0.011	-0.006	0.007	1.7
Intra-pixel, Linear Term in y	-0.058	-0.005	0.009	8.6
Intra-pixel, Linear Term in x	0.0127	-0.0010	0.0010	12.4

Supplementary Table 5. Best-fit free parameters at 4.5 μm.

Parameter	Best Fit	Low Error	High Error	SNR
Flux Ratio [%]	0.0002	-0.0032	0.0034	0.075
Star Flux [μJy]	861,900	-200	300	3,470
Ramp,Curvature	29.04	-0.08	0.11	307
Ramp,Phase Offset	0.281	-0.004	0.003	76.7
Intra-pixel, Quadratic Term in x	0.083	-0.003	0.004	22.7
Intra-pixel, Linear Term in y	0.1471	-0.0006	0.0005	267
Intra-pixel, Linear Term in x	0.0747	-0.0017	0.0022	37.7

Supplementary Table 6. Best-fit free parameters at 5.8 μm.

Parameter	Best Fit	Low Error	High Error	SNR
Eclipse Phase [orbits]	0.5873	-0.0042	0.0016	202
Flux Ratio [%]	0.033	-0.015	0.014	2.3
Star Flux [μJy]	562,190	-190	230	2,690
Ramp, Curvature	22.8	-1.2	2.2	13.3
Ramp, Phase Offset	0.293	-0.019	0.022	13.3
Intra-pixel, Quadratic Term in y	-0.032	-0.003	0.003	12.0

Supplementary Table 7. Best-fit free parameters at 8.0 μm.

Parameter	Best Fit	Low Error	High Error	SNR
Eclipse Phase [orbits]	0.5867	-0.0006	0.0006	955
Eclipse Duration [orbits]	0.0186	-0.0014	0.0015	12.9
Flux Ratio [%]	0.054	-0.008	0.008	7.3
Star Flux [μJy]	305,464	-16	16	19,500
Ramp, Curvature	41.69	-0.18	0.12	278
Ramp, Phase Offset	0.4068	-0.0008	0.0008	505

Supplementary Table 8. Best-fit free parameters at 16 μm.

Parameter	Best Fit	Low Error	High Error	SNR
Eclipse Phase [orbits]	0.5866	-0.0011	0.0009	588
Eclipse Duration [orbits]	0.0191	-0.0026	0.0020	8.2
Flux Ratio [%]	0.140	-0.025	0.029	5.3
Star Flux [μJy]	85,949	-14	15	5,880
Ramp, Linear Term	-0.082	-0.008	0.006	11.6

Supplementary Table 9. Best-fit free parameters at 24 μm.

Parameter	Best Fit	Low Error	High Error	SNR
Eclipse Phase [orbits]	0.5878	-0.0008	0.0008	747
Flux Ratio [%]	0.175	-0.042	0.041	4.2
Star Flux [μJy]	38,017	-7	7	5,310

Supplementary Figures

Supplementary Figure 5 presents the contribution functions[41] and temperature profile *vs.* pressure (or depth) for all six observed channels. Supplementary Figures 6 - 11 present histograms of the free parameter values in the MCMC chains. To remove the correlation of the steps, the plots include only a fraction of the values plotted. For the low S/N datasets such as 4.5 and 5.8 μm, the chains explore physically impossible negative eclipse depths in order to ascertain the error. Most of the histograms are roughly Gaussian in shape but some parameters exhibit non-Gaussian errors.

Supplementary Figures 12 - 17 show correlations between free parameters in a small (for clarity) but representative percentage of the Markov steps. The MCMC random walk does not always produce smooth distributions. Outlier clumps can occur where the phase space has nearby local minima. Narrow paths can result from an ergodic probability distribution, which can reach any point in the bounded phase space. The eclipse parameters are generally uncorrelated with the intra-pixel and time-varying sensitivity parameters. However, strong correlations do occur between the star flux and certain intra-pixel terms and amongst the intra-pixel terms themselves. Due to the form of Eqns. 2 and 3, we expect some degree of correlation.
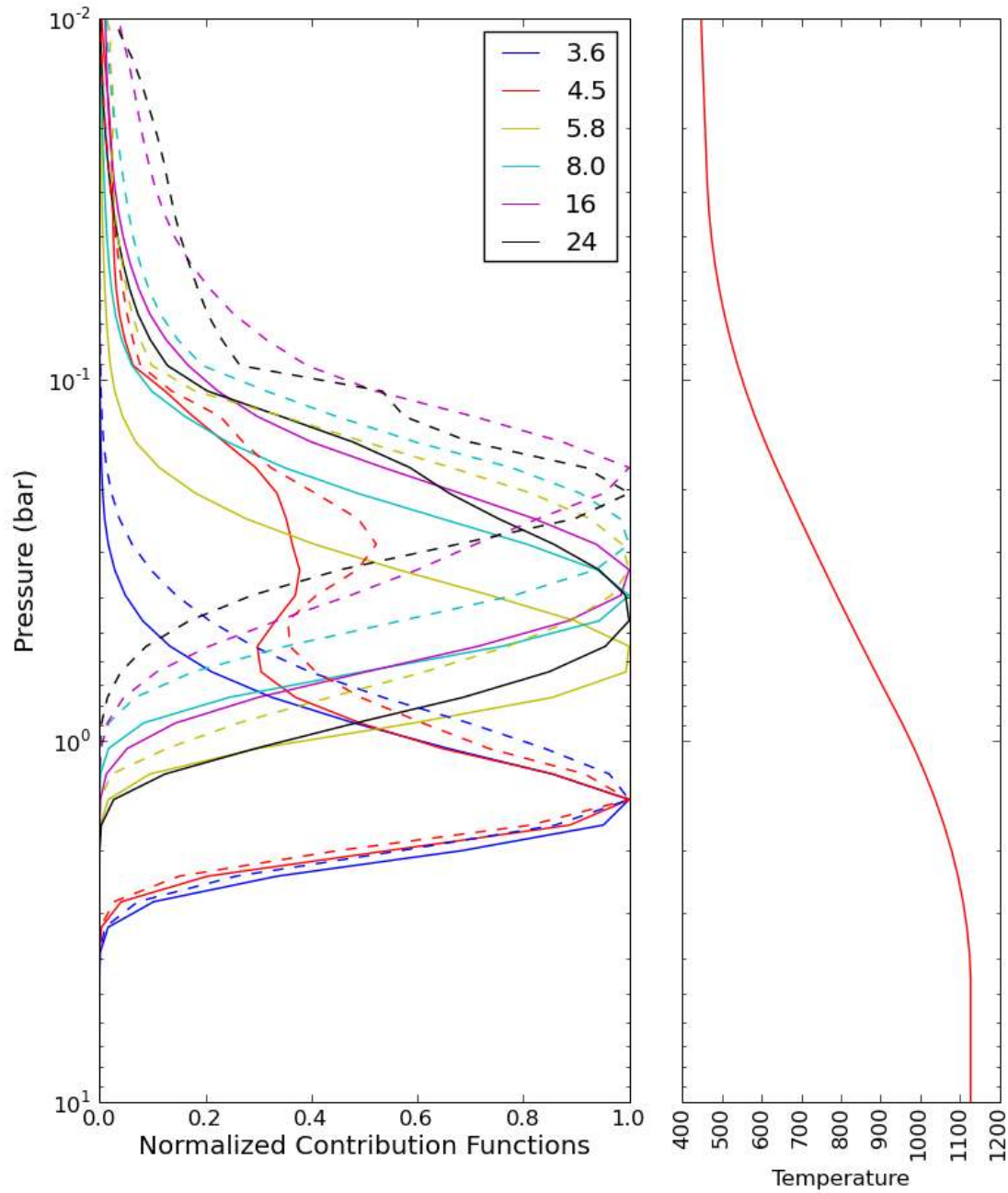
Supplementary Figure 5. Normalized contribution functions[41] of GJ 436b in all six observed channels (left) and the corresponding temperature profile (right). In the left frame, the solid lines are from the red model of Figure 2 (main paper); the dashed lines are from the blue model.
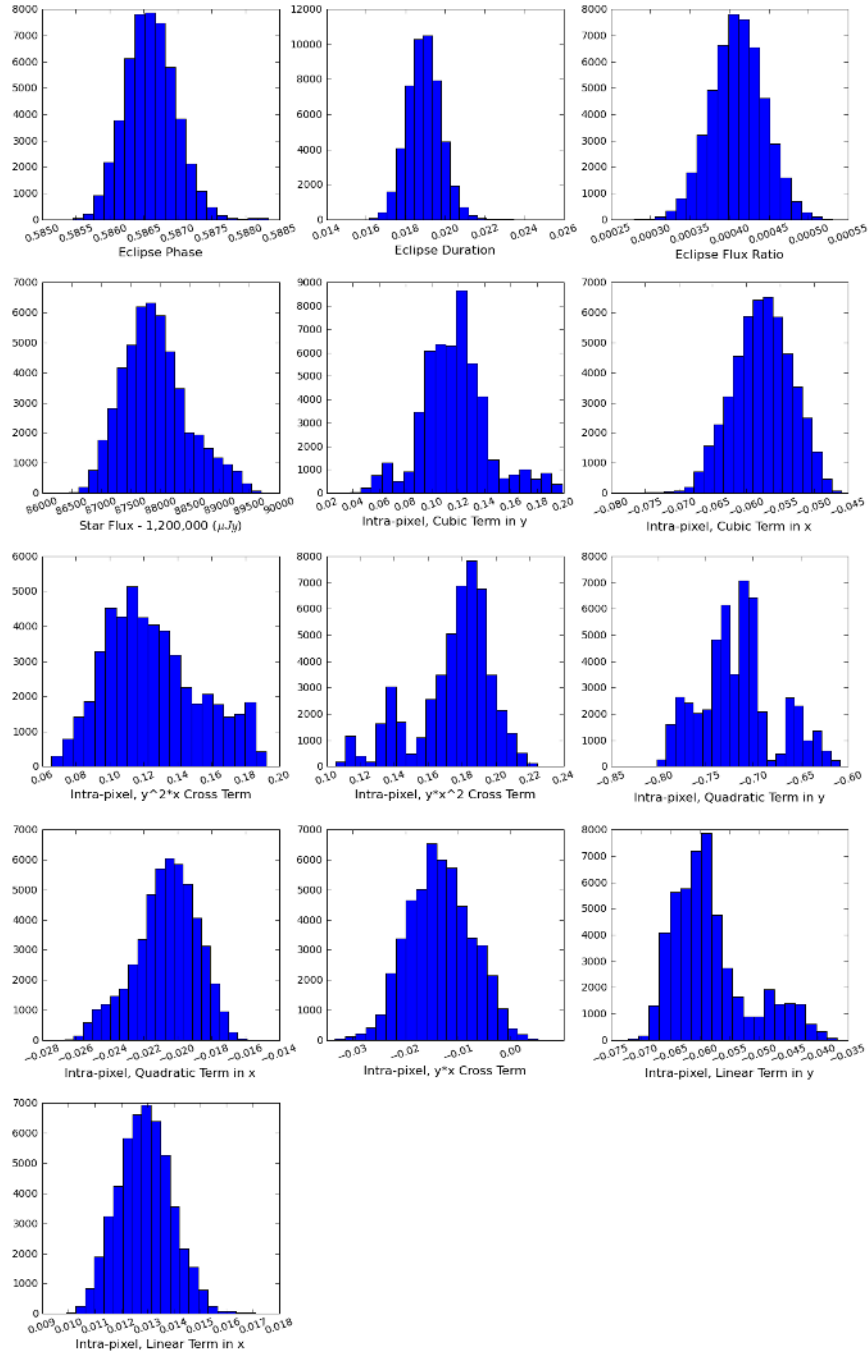
Supplementary Figure 6. Histograms of free parameters at every 100th MCMC step (out of 5×10^{6}) at 3.6 μm. The intra-pixel effect is most sensitive along the *y* axis, with the *y[2]* term dominating.
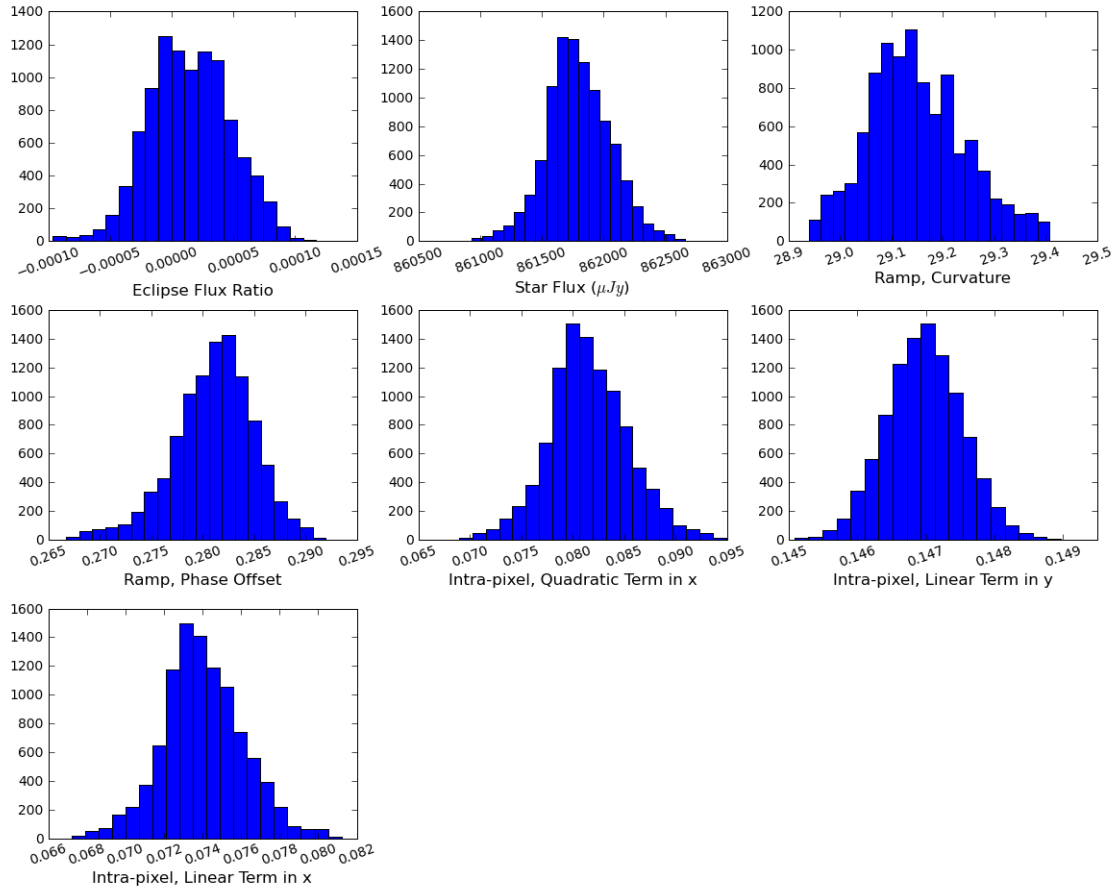
Supplementary Figure 7. Histograms of free parameters at every 100th MCMC step (out of 10^6) at 4.5 μm. The *y* term is the most dominant intra-pixel term at this wavelength.
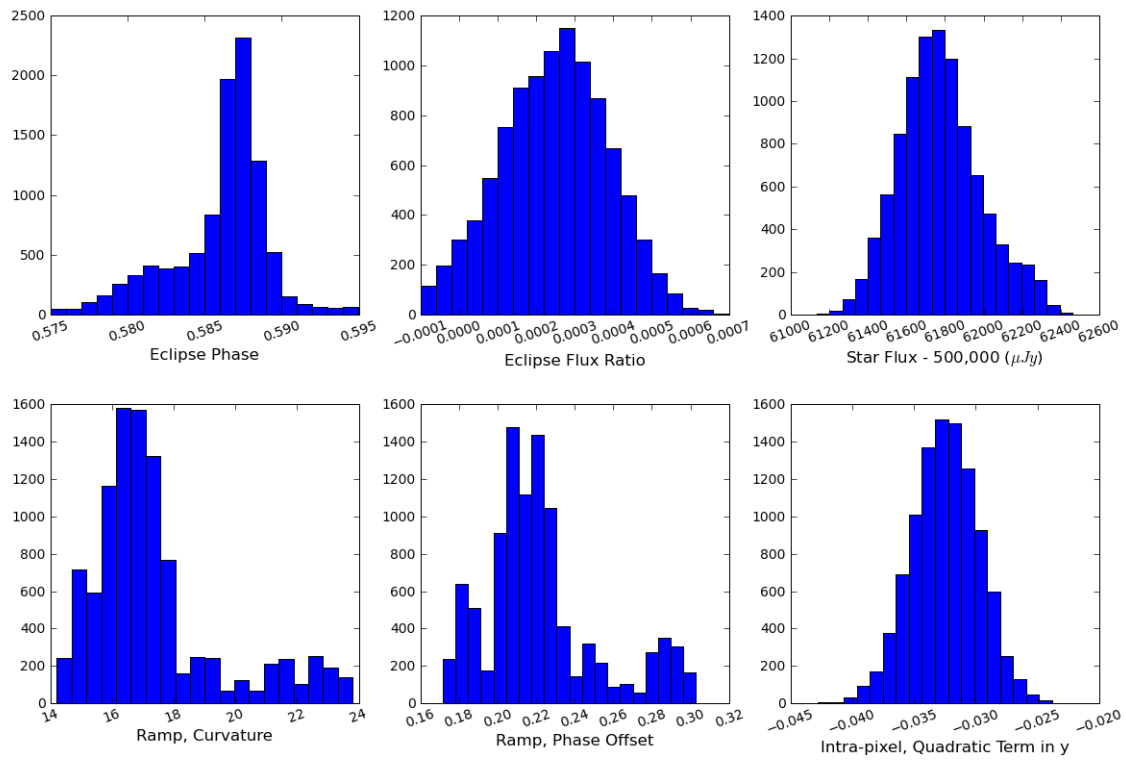
Supplementary Figure 8. Histograms of free parameters at every 100th MCMC step (out of 10^6) at 5.8 µm. Only the *y* axis intra-pixel dependence is significant.
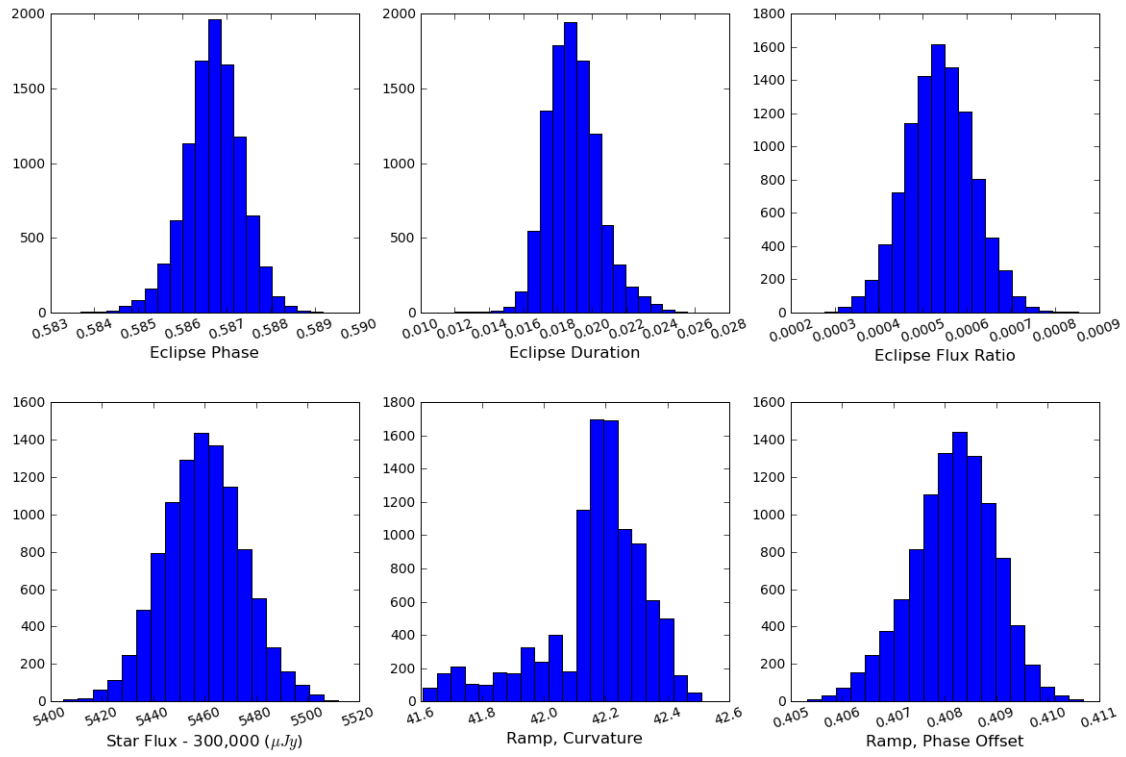
Supplementary Figure 9. Histograms of free parameters at every 100th MCMC step (out of 10^6) at 8.0 μm.
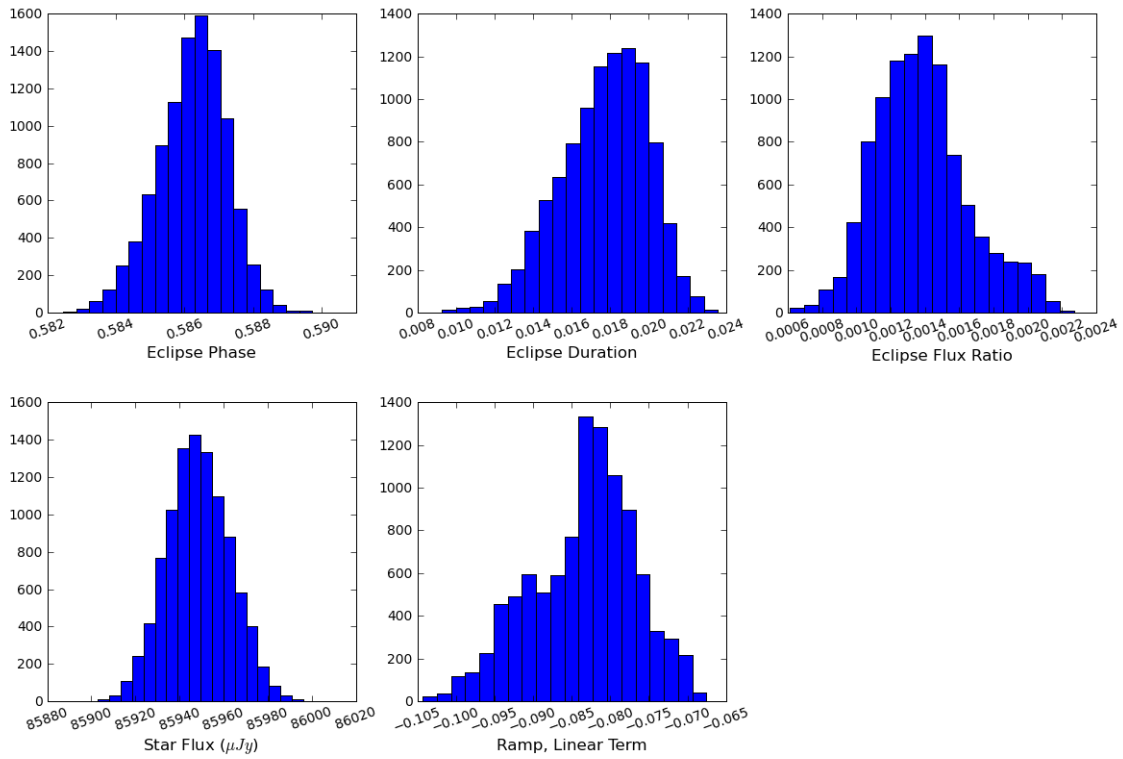
Supplementary Figure 10. Histograms of free parameters at every 100th MCMC step (out of 10^6) at 16 µm.
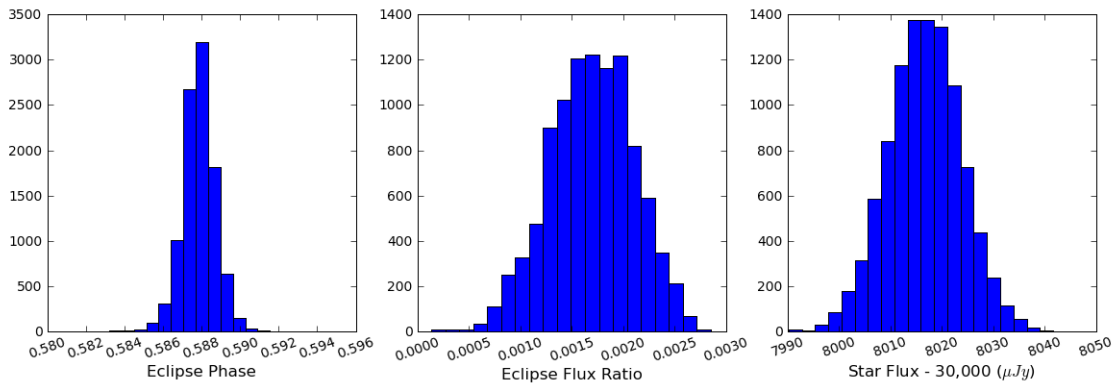
Supplementary Figure 11. Histograms of free parameters at every 100th MCMC step (out of 10^6) at 24 µm.
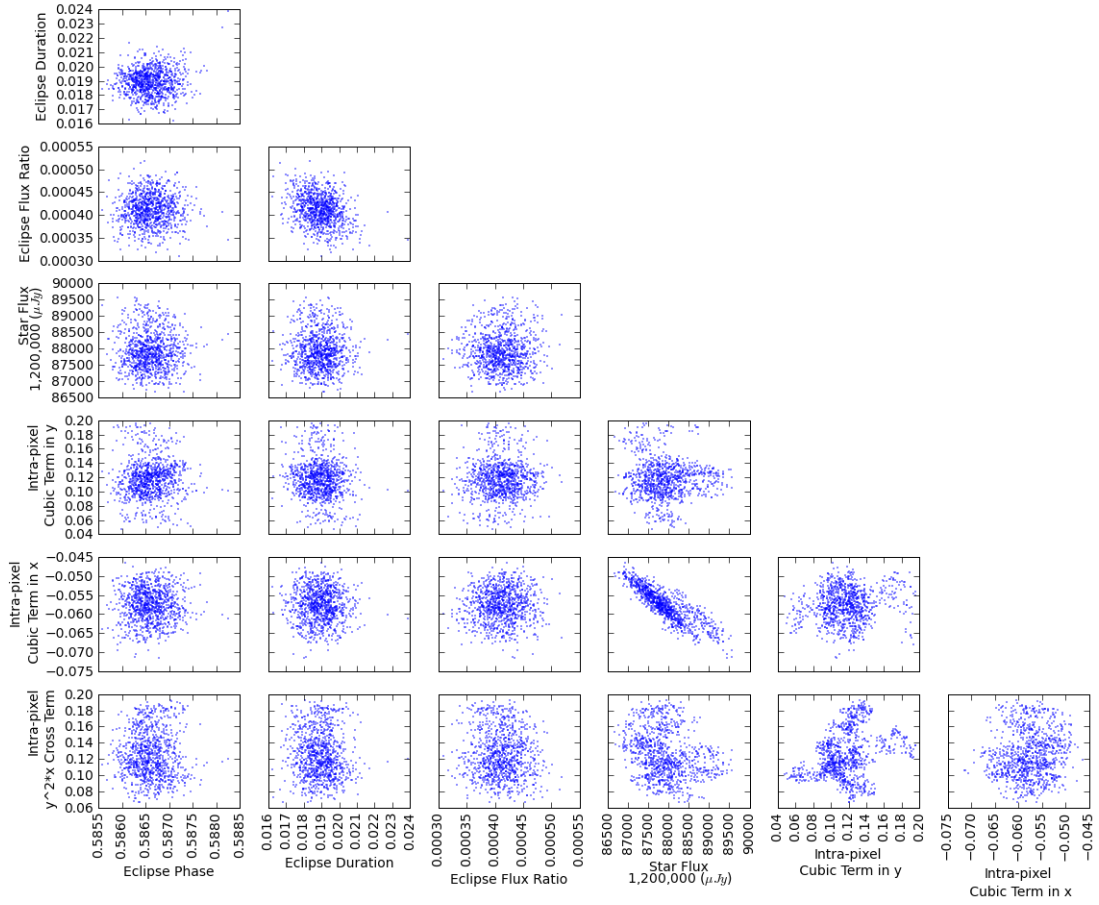
Supplementary Figure 12a. See description below.
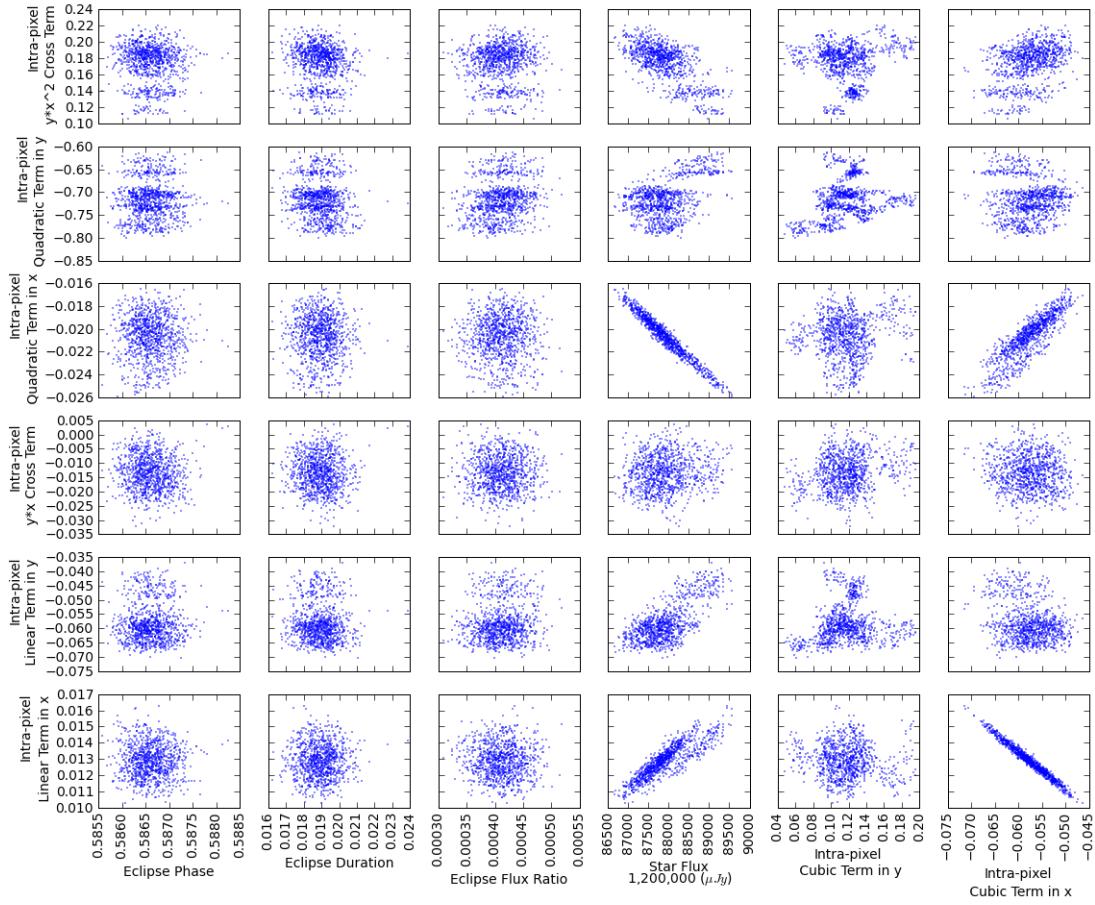
**Supplementary Figure 12b. See description below.**
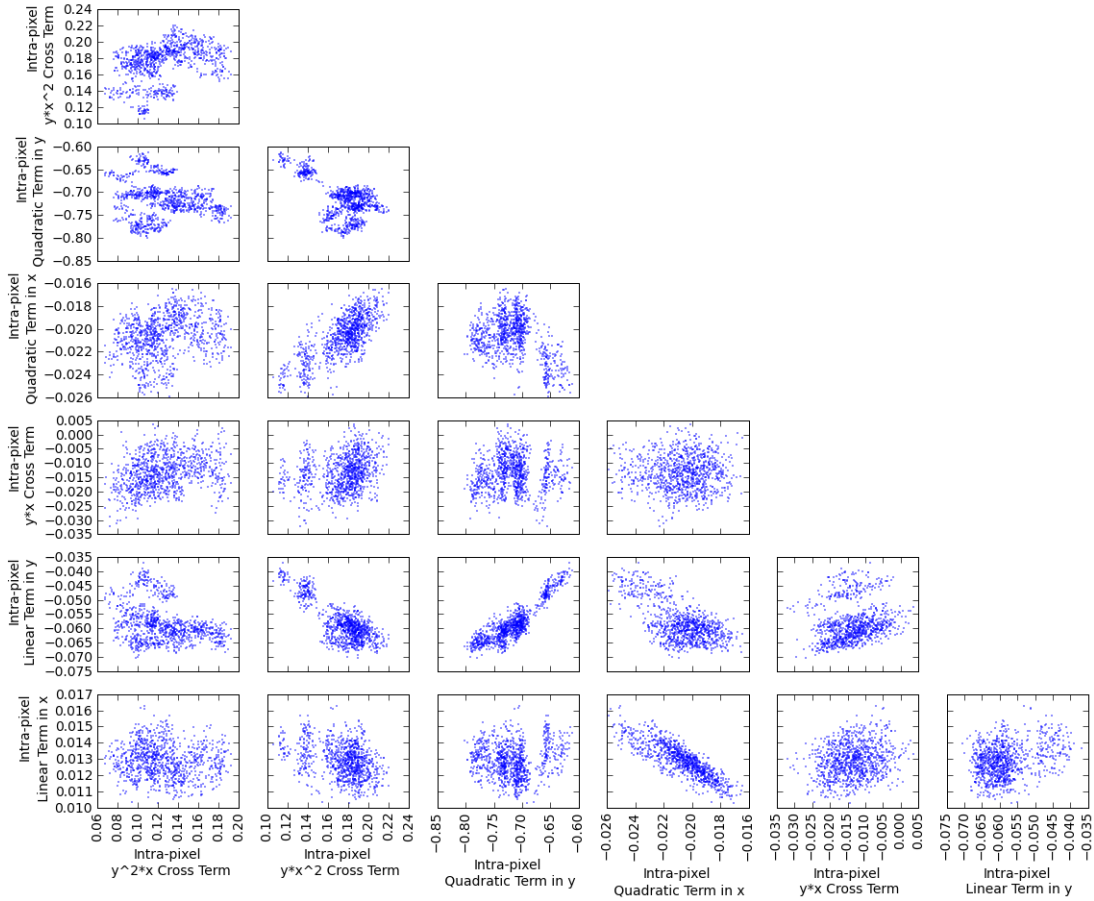
Supplementary Figure 12c.

Supplementary Figure 12. Phase-space projections for every 1000th MCMC step at 3.6 μm.   Due to the large number of free parameters in this particular model, the phase-space projections are subdivided into three figures, labeled 12a, 12b, and 12c. The y and y^2 terms are strongly correlated, with a coefficient of 0.94.   The x, x^2, and x^3 terms of the intra-pixel sensitivity show very strong correlations (>0.9 or < -0.9) amongst themselves and with the star flux. Removing any of these parameters results in a larger BIC value.
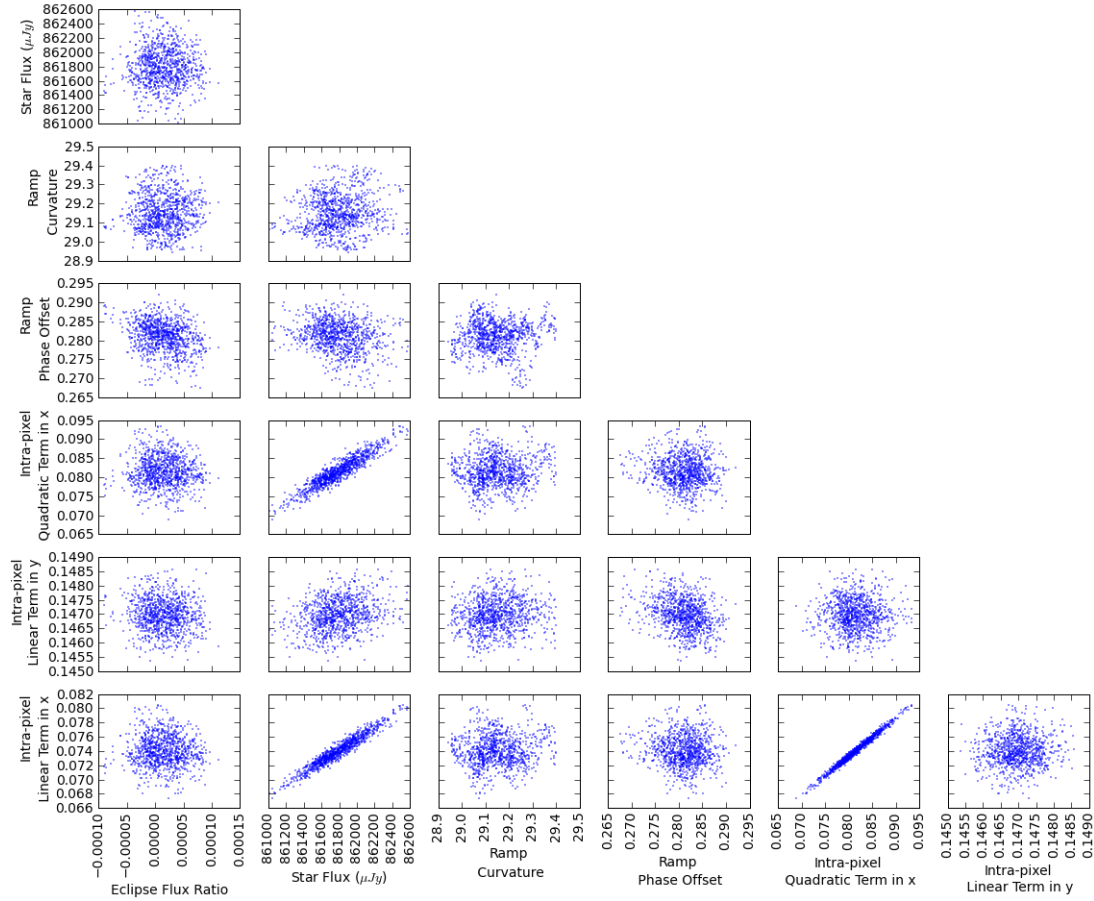
Supplementary Figure 13. Phase-space projections at every 1000th MCMC step at 4.5 μm. There are correlations of 0.96, 0.93, and 0.99 between the star flux and the x term of the intra-pixel sensitivity, the star flux and the x^2 term, and the x^2 and x terms, respectively. Again, removing one or more of these parameters results in a larger BIC value.
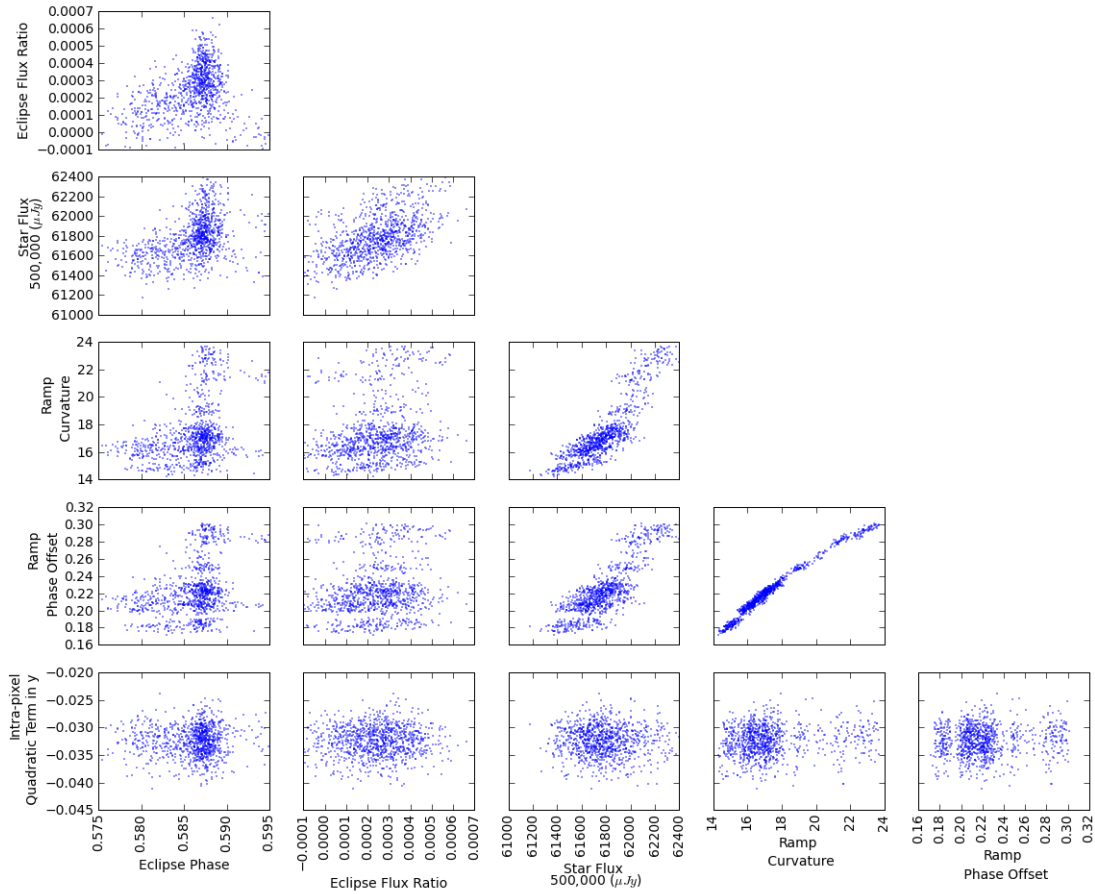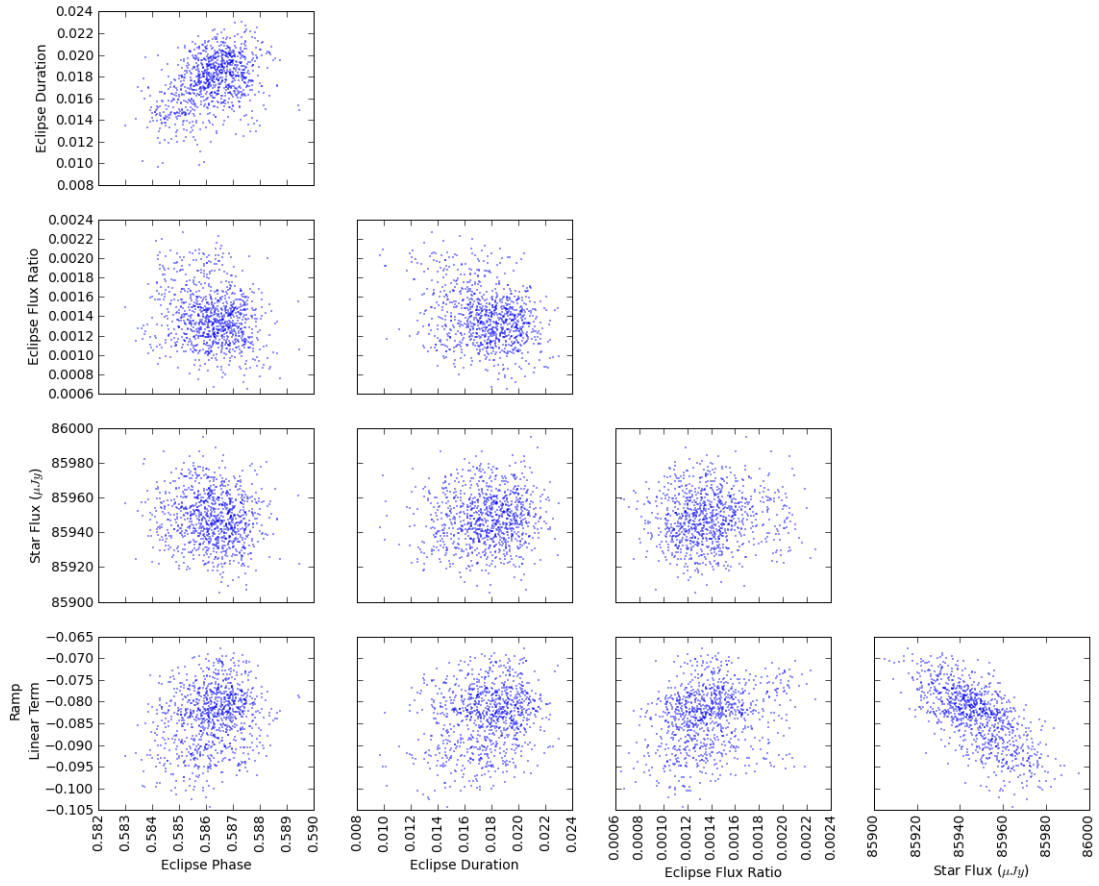
Supplementary Figure 14. Phase-space projections at every 1000th MCMC step at 5.8 μm. The ramp curvature and phase offset show a correlation of 0.97. Neither parameter can be removed without deteriorating the fit.
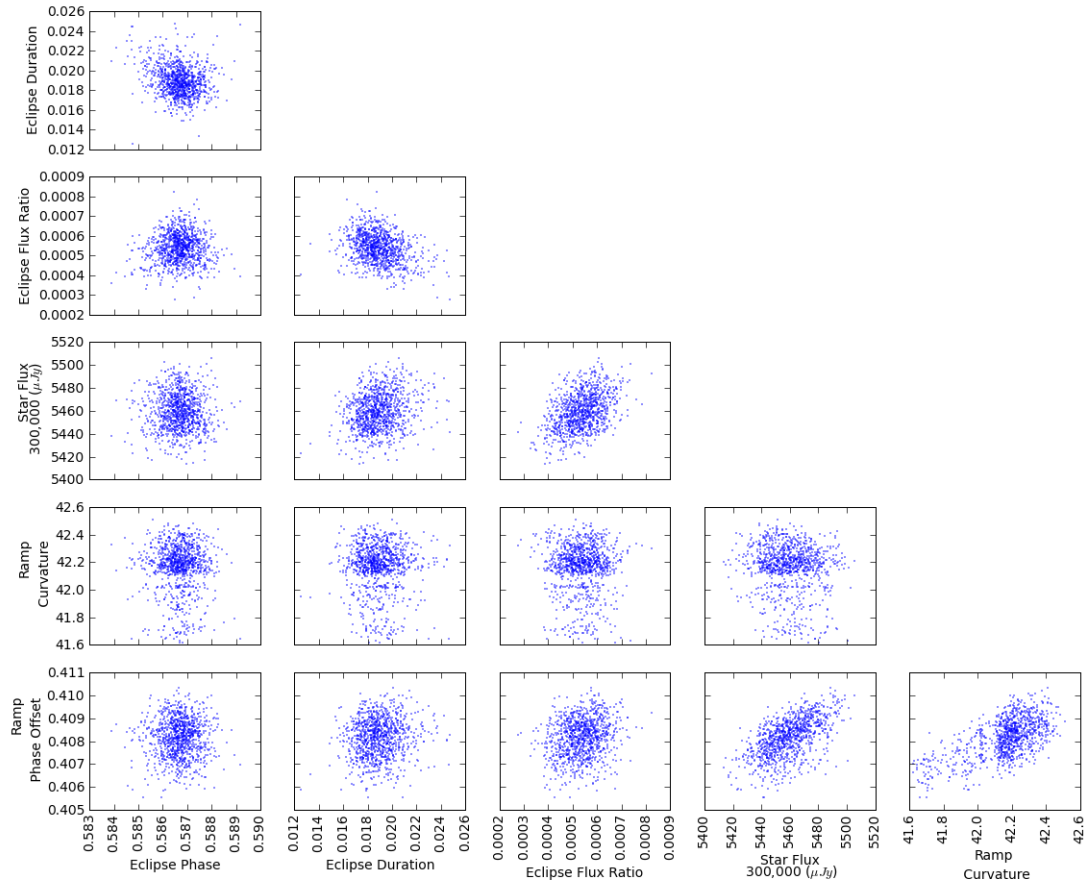
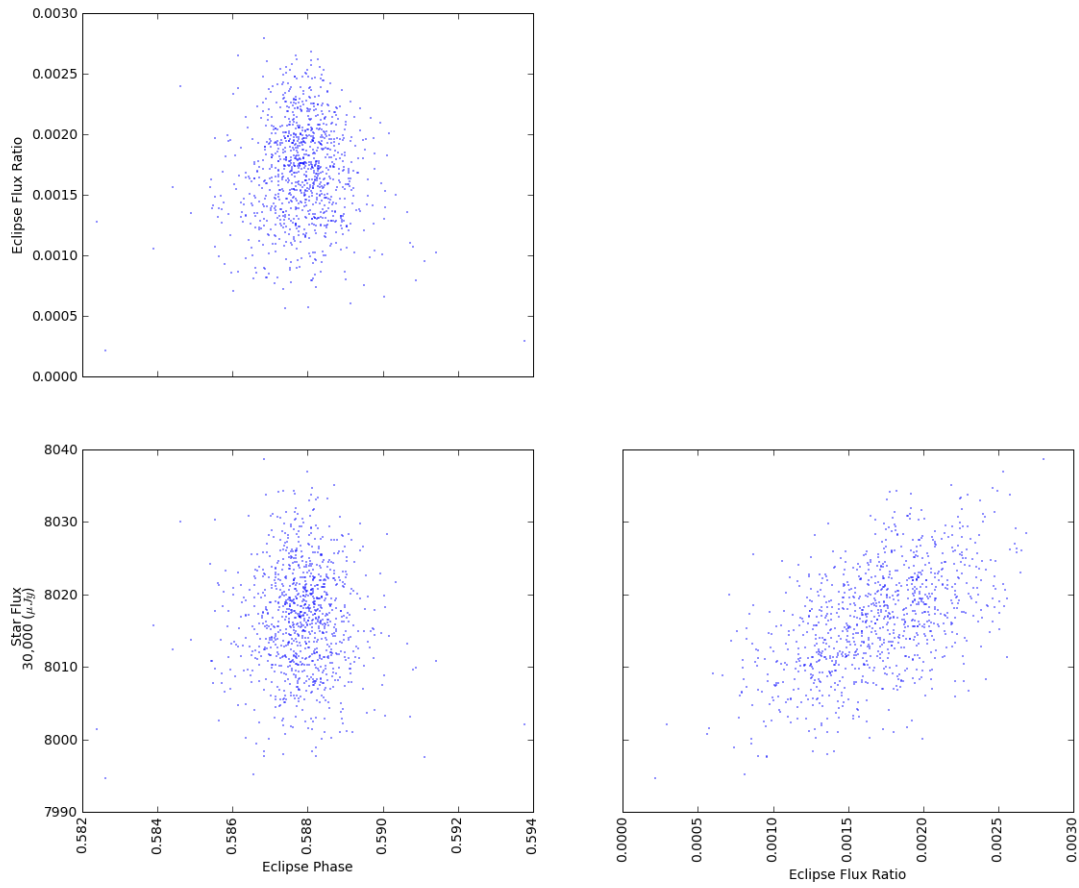**Supplementary Figure 15. Phase-space projections at every 1000th MCMC step at 8.0 μm.**

Supplementary Figure 16. Phase-space projections at every 100th MCMC step at 16 μm.

Supplementary Figure 17. Phase-space projections at every 100ᵗʰ MCMC step at 24 μm.

Supplementary References:

31. Fazio, G. G. *et al.* The Infrared Array Camera (IRAC) for the Spitzer Space Telescope. *Astrophy. J. Suppl. Ser.* **154**, 10–17 (2004). arXiv:astro-ph/0405616.

32. Horne, K. An optimal extraction algorithm for CCD spectroscopy. *Publ. Astron. Soc. Pac.* **98**, 609–617 (1986).

33. Howell, S. B. *Handbook of CCD Astronomy* (Cambridge University Press, 2000).

34. *http://ssc.spitzer.caltech.edu/irac/psf.html*.

35. Houck, J. R. *et al.* The Infrared Spectrograph (IRS) on the Spitzer Space Telescope. *Astrophy. J. Suppl. Ser.* **154**, 18–24 (2004). arXiv:astro-ph/0406167.

36. Rieke, G. H. *et al.* The Multiband Imaging Photometer for Spitzer (MIPS). *Astrophy. J. Suppl. Ser.* **154**, 25–29 (2004).

37. Schwarz, G. Estimating the dimension of a model. *The Annals of Statistics* **6**, 461–464 (1978). URL http://www.jstor.org/stable/2958889.

38. Liddle, A. R. Information criteria for astrophysical model selection. *Mon. Not. R. Astron. Soc.* **377**, L74–L78 (2007). arXiv:astro-ph/0701113.

39. Rubenstein, E. P. & Schaefer, B. E. Are Superflares on Solar Analogues Caused by Extrasolar Planets? *Astrophys. J.* **529**, 1031–1033 (2000). arXiv:astro-ph/9909187.

40. Rossiter, R. A. On the detection of an effect of rotation during eclipse in the velocity of the brigher component of beta Lyrae, and on the constancy of velocity of this system. *Astrophys. J.* **60**, 15–21 (1924).

41. Knutson, H. A. *et al.* Multiwavelength Constraints on the Day-Night Circulation Patterns of HD 189733b. *Astrophys. J.* **690**, 822–836 (2009). 0802.1705.